Whispering-Gallery-Mode Sensors for Biological and Physical Sensing

Deshui Yu[1], Matjaž Humar[2,3,4] ✉, Krista Meserve[5], Ryan C. Bailey[5] ✉, Síle Nic Chormaic[6] ✉, and Frank Vollmer[1] ✉

[1]Living Systems Institute, Physics and Astronomy, University of Exeter, Exeter, UK
[2]Condensed Matter Department, J. Stefan Institute, Ljubljana, Slovenia
[3]Faculty of Mathematics and Physics, University of Ljubljana, Ljubljana, Slovenia
[4]CENN Nanocenter, Ljubljana, Slovenia
[5]Department of Chemistry, University of Michigan, MI USA
[6]Okinawa Institute of Science and Technology Graduate University, Onna, Okinawa Japan
✉*e*-mail: matjaz.humar@ijs.si; ryancb@umich.edu; sile.nicchormaic@oist.jp; f.vollmer@exeter.ac.uk

Abstract | The term whispering gallery modes (WGMs) was first introduced to describe the curvilinear propagation of sound waves under a cathedral dome. The physical concept has now been generalized to include light waves that are continuously reflected along the closed concave surface of an optical cavity such as a glass microsphere. The circular path of the internally reflected light results in constructive interference and optical resonance, a morphology-dependent resonance that is suitable for interferometric sensing. WGM resonators are miniature micro-interferometers that use the multiple-cavity passes of light for very sensitive measurements at the micro- and nanoscale, including single molecules and ions measurements. This Primer introduces various WGM sensors based on glass microspheres, microtoroids, microcapillaries and silicon microrings. We describe the sensing mechanisms including mode splitting and resonance shift, exceptional-point-enhanced sensing, and optomechanical and optoplasmonic signal transductions. Applications and experimental results cover *in-vivo* and single-molecule sensing, gyroscopes and microcavity quantum electrodynamics. Data analysis methods and limitations of the WGM techniques are also discussed. Finally, we provide an outlook for molecule, *in-vivo* and quantum sensing.

[H1] Introduction

Optical microcavities confine a light wave within a microscale volume by the reflection of light. An example for this is the Fabry–Pérot resonator composed of two opposing mirrors. The constructive interference of the light propagating back and forth between two mirrors builds up intensity at certain optical wavelength, resulting in optical resonance. The optical resonance is observed as a Lorentzian-shaped spectral feature, for example, in the transmission or reflection spectrum of the microcavity. In the case of whispering-gallery-mode (WGM) microcavities (FIG.1, Box 1) , the light is confined within dielectric microstructures, for example glass microspheres with a diameter of about 10^2 µm, by means of successive near-total internal reflections **[G]** that occur at the interface between the microcavity and its surrounding[1]. By using an appropriate optical coupler[2], only the evanescent field **[G]** extends into the surrounding medium from where the microcavity is excited.

Owing to this unique light-confinement mechanism, WGM microcavities have small effective mode volumes **[G]** V_{eff} while still preserving ultrahigh quality (Q) factors[3] **[G]** (Supplementary Note 1). The resultant large Purcell factor[4] **[G]** $F_{\text{P}} \equiv (3/4\pi^2)(Q/V_{\text{eff}})(\lambda_0/n_{\text{i}})^3$ (for example, 2.5×10^5 in REF.[5]), where λ_0 is the WGM resonance wavelength and n_{i} the refractive index of the microcavity's material, is highly desirable to achieve strong light-matter interaction that enhances the sensor's sensitivity. For F_{P} greatly exceeding unity, the local density of optical states is significantly tailored by the microcavity so that an emitter, such as an atom or a molecule located inside or close to the microcavity, experiences an accelerated spontaneous emission[6,7]. Even one emitter may affect the intracavity field and lead to a notable signal that can be captured by a photodetector. The prolonged time of the light circulating inside a WGM microcavity on resonance also results in a large number of roundtrips measured by the finesse $\mathcal{F}$ **[G]** of the microcavity (with $\mathcal{F}$ over 10^6 for a glass microsphere[8] for example). When a biological entity such as a molecule lands on the microcavity's surface, the circulating light interacts with this entity $\mathcal{F}$ times, boosting the sensing signal. In addition, WGM microcavities possess the advantages of relatively ease of fabrication, small footprint and low cost. All these features contribute to an extensive application of WGM microcavities in biochemical, temperature and mechanical sensing[9], where the environmental perturbations that influence the spectral properties of WGMs such as mode splitting[10], resonance wavelength shift[11] and broadening[12], can be monitored in real time.

In biochemical sensing, small perturbations of the optical path length that are induced by adsorbing molecules onto the surface of a WGM microcavity can be measured with an exceedingly high sensitivity from the optical resonance shift[11]. Single-molecule detection is achieved by hybridizing plasmonic metal nanoparticles with WGM microcavities[13]. Although metal nanoparticles slightly degrade the confinement of light, the hybridization concentrates a fraction of the light at the microcavity's surface where the molecules in solution are detected and results in a benefit for sensing. When a molecule enters the plasmonic hotspot **[G]** by, example, binding to a metal nanoparticle or a receptor molecule that has been immobilised on the surface of a metal nanoparticle, it gives rise to a WGM resonance shift that is typically on the order of femtometres[14]. Different from other single-molecule techniques, WGM sensors operate in a label-free fashion with a time resolution of microseconds.

In addition to optoplasmonic WGM sensors, other types of microstructures have also been employed in biosensing. Hollow WGM microresonators are made from thin-walled glass capillaries and filled with water for molecule and particle detection via the evanescent field[15,16]. Multiplexed silicon ring resonators are integrated with microfluidics for high-throughput sensing of specific biomolecular interactions[17-19]. In bio-integrated photonics, WGM microcavities with optical gains **[G]**

are being used as free floating probes to study live cells and for *in vivo* applications[20-24], where the lasing spectrum of a WGM sensor is recorded under a sufficiently high excitation power. This narrow emission spectrum enables spectral multiplexing[25], operation within highly scattering and absorbing media, and simultaneous barcoding **[G]** and imaging. Changes in the WGM lasing spectrum have been used for detecting the contraction of muscle cells[21] for example. WGM fluorescence and lasing spectra are unique barcodes that can identify a sensor, allowing for parallel tracking of multiple sensors[26].

In physics, WGM microcavities have been used for various important and fundamental topics such as on-chip light sources[27], cavity optomechanics[28], non-Hermitian physics[29], quantum metrology with WGM microcombs[30] and cavity quantum electrodynamics (QED)[31]. Due to small mode volumes and ultrahigh Q factors, the thresholds of WGM microlasers are ultralow[32] and potentially operate as light sources in photonic integrated circuits[33]. Experiments have succeeded in cooling the mechanical vibration of a microcavity close to the quantum-mechanical ground state[34,35]. Coupled microcavities provide a vivid platform for studying spontaneous parity-time symmetry breaking[36], nonreciprocity of light propagation[37], and novel optical phenomena around exceptional points[38]. Frequency microcombs in monolithic structures are portable and robust and have extensive application in chip-scale optical atomic clocks[39]. Finally, WGM microcavities are an excellent candidate to achieve strong coupling between an optical mode and a quantum emitter[40,41].

This Primer focuses on the introduction of sensing applications of WGM microcavities in biochemistry and physics[42]. It is targeted at early career researchers from biology and physics to provide a broad insight into the setup and potential applications of WGM sensors in their own research fields. We start by introducing different WGM instruments for the detection of biological and physical entities and discuss various sensing mechanisms in the Experimentation section. In the Results section, we focus on different types of WGM sensing signals that are obtained for the example of single-molecule detection. The Applications section reviews biological and physical experiments including *in vivo* sensing, gyroscopes and microcavity QED. Next, we discuss the limitations of current WGM sensors, measurement reproducibility and data deposition, before ending with an outlook on the future of WGM optoplasmonic single-molecule, *in vivo* and quantum sensing.

[H1] Experimentation

A typical WGM-microcavity-based sensor consists of a low-noise pump source, a high Q microcavity that is evanescently coupled with an optical fibre/prism and a spectrum analyser. Usually, sensors operate in a passive fashion, where single nanoparticles/molecules are detected using the sensor's

transmission spectrum. Recently, active sensors with optical Raman gain have also been demonstrated[43,44].

[H2] Making WGM microcavities

Various applications of WGM microcavities in biological and physical sensing require different microcavity materials and geometries. The solid-state WGM microstructures include glass microspheres[1] (FIG. 1a), hollow microbottles[15,16]/optofluidic microbubbles[45-47] (FIG. 1b) and microtoroids[48] (FIG. 1c). WGMs in a microstructure may be analytically investigated in a precise[49,50] or approximate[15,51-55] manner by using a MATLAB toolbox[56]. Several numerical tools, such as Lumerical, based on the finite-difference time-domain approach, and COMSOL Multiphysics, based on the finite element method, are also usually applied to study WGMs. The high symmetry of solid microspheres allows an analysis on WGMs in a rigorous way (Supplementary Note 2). The Q factor of such microspheres in air ranges from 10^8 to 10^9 (REFS[1,57]) and degrades to $10^5 \sim 10^6$ in an aqueous environment[58]. When the fluid is inside the WGM resonator, a similar reduction in Q factor due to fluid absorption can be expected[59,60]. Since the physical dimension of a microsphere relies solely on its radius R, all optical properties of a WGM, such as the resonance frequency $\omega_0 = 2\pi c/\lambda_0$ and the Q factor, are directly related to R, leading to limited controllability since different optical properties cannot be controlled independently. While hollow resonators (FIG. 1b) are quite similar to microspheres in their mode structure, the electric field distribution strongly depends on an additional degree of freedom through the wall thickness, providing an element of control that can lead to improved performance in sensing once the quasi-droplet regime **[G]** is accessed[59,61,62]. In contrast, microtoroids provide both transverse and vertical spatial confinement to the light field, simplifying the modal spectrum compared to microspheres and improving controllability[48]. A typical microtoroid is composed of a glass ring cavity that is suspended over a silicon pillar by a silica membrane (FIG. 1c). The ring cavity is characterized by a major radius R and a minor radius a, which can be controlled independently in experiments. Silica microtoroids combine an ultrahigh Q factor comparable to that of microspheres and a mode volume V_{eff} smaller than that of microspheres with the same R (REFS[5,63]).

WGM microcavities with smooth surfaces can be produced by using the surface tension of liquids/melts to make microdroplets[64,65], microspheres[1,57] and microbubbles[45,66], and to develop wafer-scale processing methods for microdisks[67,68] and microtoroids[48]. Using liquid surface tension is simple and does require a skilled technician. For instance, glass microspheres can be easily fabricated by melting the tip of a silica fibre with a high-power CO_2 laser or an oxygen-butane microflame torch, where the surface tension produces spherical shapes[11]. The root-mean-square roughness of a typical surface finish nearly reaches the atomic scale at approximately 2 nm[8].

Optofluidic resonators **[G]** typically require several fabrication steps but are still relatively easy to make. For a quasi-droplet resonator, a section of glass capillary is generally either pre-etched by using aqueous hydrofluoric acid[47,61,69,70] or pre-tapered by using a gas torch[66,71] to reduce the wall thickness prior to pressure expansion. The capillary is heated by using an arc discharge[72], hydrogen-oxygen torch[70] or a CO_2 laser[45,66] while a pressurized air system is used to expand the molten glass to form the bottle or bubble shape. The thickness of the glass wall is crucial to ensure high sensitivity and can be determined theoretically[45,73,74] through non-destructive confocal imaging[75] or destructive scanning electron microscope imaging[61,76]. In contrast, wafer-based fabrication, which combines lithography, etching and a selective reflow process (Supplementary Note 3), is usually adopted to produce (ultra)high-Q polymer/silica microcavities-on-a-chip[77,78]. Lithographical fabrication is also used to produce a chain of surface-nanoscale-axial-photonics microresonators along an optical fiber[79] with a fabrication precision at the sub-angstrom level. In comparison to polymers, glass has high chemical resistance to harsh environments, such as aggressive solvents at elevated temperatures, and is the right material for fabricating sensors. Recently, the fabrication of all-glass microtoroids has been reported[80].

The evanescent field of a microcavity allows for light to be coupled into/out of the microcavity through fibre[81,82], prism[3,83,84] or on-chip waveguide[85] couplers. Prism and waveguide couplers are more stable than fibre couplers[86]. However, the application of a prism coupler is restricted by its bulkiness and feeding light into a waveguide requires extra optical devices and techniques. Tapered fibre couplers with subwavelength spatial separation between the microcavity and the tapered fibre's thinnest section give the most efficient coupling (greater than 99.9 percent[87]). However, tapered fibres are extremely fragile and their optical properties can deteriorate within several hours due to dust deposition. Additionally, tapered fibres are susceptible to environmental perturbations, such as airflow disturbance and mechanical vibrations. Decreasing the fibre-microcavity distance does not always enhance the coupling efficiency. There exists a critical coupling point at which the coupling efficiency is maximized (BOX 2, Supplementary Fig. 2).

[H2] Biochemical sensing

Typically, WGM-microcavity-based sensing mechanisms include monitoring the mode splitting caused by the scatterer-induced coupling between two degenerate **[G]** counter-propagating WGMs[10], tracking the resonance shift induced by the change in the local refractive index[88] and tracking the spectral broadening that originates from the extra dissipation channel opened by analyte particles[12]. Recently, a mode-distribution measurement based on surface-nanoscale-axial-photonics microresonators has also been proposed for sensing applications, especially detecting the

position and displacement of individual particles. More details on this mechanism can be found in REF.[89].

[H3] Mode splitting

For a bare microcavity, a pair of degenerate clockwise and counter-clockwise WGMs correspond to the same Lorentzian-shaped peak/dip occurring at the resonance frequency ω_0 in the transmission spectrum of the microcavity. When a Rayleigh scatterer, whose size is much smaller than the mode wavelength λ_0, enters the evanescent zone of the microcavity, two WGMs are indirectly coupled with each other due to the scatterer-induced backscattering[90] (FIG. 2a), that is a portion of the clockwise light is scattered into the counter-clockwise WGM and vice versa. As a result, the degeneracy between two WGMs lifts and gives rise to a mode splitting Δ in the transmission spectrum[10,81] (FIG. 2b). Single-nanoparticle events can be identified by monitoring the mode splitting in real time.

The mode splitting Δ depends linearly on the excess polarizability **[G]** α_{ex} of the scatterer, that is the amount of the scatterer's polarizability in excess of the surrounding medium. In sensing, the medium is mostly water and the mode splitting is $\Delta = \alpha_{ex}\omega_0/V_{eff}$, where V_{eff} isthe effective mode volume of WGMs. For a spherical scatterer with a radius a, α_{ex} takes the form $\alpha_{ex} = 4\pi a^3(\epsilon_s - \epsilon_o)/(\epsilon_s + 2\epsilon_o)$, where ϵ_s and ϵ_o are the relative dielectric permittivities of scatterer and environmental medium respectively. The mode volume V_{eff} is defined based on the light intensity at the scatterer's position $\mathbf{r}_0$,

$$V_{eff} = \int \epsilon(\mathbf{r})|\mathbf{E}(\mathbf{r})|^2 d\mathbf{r}/\epsilon(\mathbf{r}_0)|\mathbf{E}(\mathbf{r}_0)|^2. \quad (1)$$

Here, $\epsilon(\mathbf{r})$ represents the spatial distribution of the relative permittivity and $\mathbf{E}(\mathbf{r})$ denotes the WGM electric field. In addition to the mode splitting, the Rayleigh scattering **[G]** also causes an extra spectral broadening $\Gamma = \alpha_{ex}^2\omega_0^4/6\pi(c/n_o)^3V_{eff}$ with $n_o = \sqrt{\epsilon_o}$. The resolvable mode splitting demands[58] $\Delta > \kappa + \Gamma$. For example, let us consider a polystyrene nanoparticle with $a = 150$ nm and $\epsilon_s = 2.52$. In air $\epsilon_o = 1$, the excess polarizability α_{ex} at $\lambda_0 = 1550$ nm is evaluated as $\alpha_{ex} = 1.4 \times 10^{-20}$ m^3. When the nanoparticle is deposited onto a silica microcavity with $V_{eff} = 5 \times 10^{-13}$ m^3, the scatterer-induced mode splitting reaches $\Delta = 2\pi \times 5.4$ MHz and the Rayleigh scattering rate is $\Gamma = 2\pi \times 0.3$ MHz. Thus, to observe the mode splitting the microcavity Q factor should exceed 4×10^7.

In experiments, the transmission spectrum of a microcavity is captured by a photoreceiver connected to an oscilloscope. A nozzle that is placed close to the microcavity delivers dielectric nanoparticles **[G]** to the evanescent zone of the microcavity. FIGURE 2b illustrates an example of the transmission spectrum of a microcavity under consecutive nanoparticle deposition events. As the nanoparticle number increases, both spectral dips broaden and deteriorate the resolution of the

doublet lineshape. It should be noted that successive single-nanoparticle events do not always increase the mode splitting since the specific interaction between microcavity and newly deposited nanoparticles also depends upon the positions of previously deposited nanoparticles[10].

The mode splitting allows for a self-referencing detection scheme, where one split mode can act as a reference for the other split mode since both split modes experience the same condition. This scheme isas a robust tool to suppress environmental noises such as temperature fluctuations[91]. Besides passive detection, mode-splitting sensing is also applicable to active microcavities with optical gains[43,92]. Single-nanoparticle/molecule detection is achieved by monitoring the beat frequency **[G]** of two split-mode lasers. The spectral linewidth strongly narrows under the lasing action, thereby improving the resolution limit. To date, mode-splitting sensing has been demonstrated mainly for silica microspheres/microtoroids detecting single polystyrene nanoparticles in air[10,58,93]. When operating in an aqueous environment, microcavities suffer from a strong degradation of the Q factor due to the increased absorption loss in water[93]. The mode-splitting resolvability criterion $\Delta > \kappa + \Gamma$ significantly restricts the application of the mode-splitting mechanism in biochemical sensing of small-sized molecules in liquid solutions. In addition to one-microcavity-based sensors, mode splitting in coupled microresonators can also be used for sensing in an either permanent[94] or tunable[95] manner.

[H3] Resonance shift

A more general sensing mechanism is the resonance wavelength shift $\Delta\lambda$ of a high-Q WGM caused by the variation in the refractive index of the surrounding medium of the microcavity (FIG. 2c,d). This sensing method is applicable in both air and aqueous environments. In bulk sensing, a microcavity is entirely immersed in a liquid sample, whose refractive index is directly related to the analyte concentration. For example, the refractometric sensitivity of a silica microsphere with $R = 50$ μm in an aqueous environment is estimated as 80 nm per refractive index units (RIU) around $\lambda_0 = 1550$ nm. Since the variations in concentrations of different substances in a solution may result in the same bulk-refractive-index change, the target substance cannot be distinguished solely by the WGM resonance shift. This issue can be solved by functionalizing the microcavity's surface with receptor molecules that can selectively capture specific ligand molecules. As a result, the mode resonance shift primarily reveals the refractive index change in the vicinity of the microcavity surface in a surface sensing[96] manner. Today, resonance-shift sensing has reached the single-molecule level[97] and canmonitor single-molecule biochemical reactions.

Optofluidic resonators have some clear advantages for biochemical sensing. Because of the hollow nature of such devices, they can be integrated with microfluidic systems, for which they have increased sensitivity in the quasi-droplet regime and still maintain very high Q factors with low

optical mode volumes. Besides biosensing, optofluidic sensors can be also used to detect dramatically small alterations in microcavity materials. Recently, the slow optical cooking effect has been observed[98].

When a molecule with an excess polarizability α_{ex} is deposited onto a WGM microcavity's surface, the WGM resonance wavelength λ_0 experiences a shift[99]

$$\Delta\lambda/\lambda_0 = \alpha_{ex}/2V_{eff}. \quad (2)$$

A small V_{eff} enhances the sensitivity $\Delta\lambda/\lambda_0$. A straightforward way to suppress V_{eff} is to reduce the microcavity's radius R. Both theory[88] and experiment[100] have shown a scaling of $(\Delta\lambda/\lambda_0)\sim R^{-5/2}$. However, reducing R also degrades the microcavity Q factor because of the increased radiation and surface scattering losses. An alternative way to suppress V_{eff} is enhancing the evanescent field at the position of dielectric molecule. Recently, the localized surface plasmon resonance **[G]** of metal nanostructures has been hybridized with WGM microcavities to boost the near-field coupling between single molecules and microcavities[14,101-108], leading to optoplasmonic sensors (FIG. 2c). Indeed, the localized surface plasmon resonance allows for light confinement beyond the diffraction limit[109], boosting the near-field intensity by a factor of over 10^3.

FIGURE 2c illustrates a general optoplasmonic sensing scheme, where a silica microsphere is immersed in a solution containing analyte molecules and a robust prism coupler is utilized to evanescently excite WGMs in a microsphere. Metal nanoparticles, such as gold nanorods, are permanently adsorbed onto the microsphere's surface. Despite the near-field enhancement, metal nanoparticles inevitably suffer from Ohmic losses **[G]**, opening an extra decay channel for the intracavity field. The related Q-factor degradation of the microcavity depends on the number of adsorbed metal nanoparticles and their alignment direction. Cetrimonium bromide-capped gold nanorods are often used for the plasmonic enhancement of WGM evanescent fields[14,101,106,107,110]. The length of individual nanorods is chosen such that the longitudinal plasmon resonance wavelength approximately matches the WGM wavelength. The nanorods are attached to the WGM microcavity by adsorption from an aqueous solution at the pH of 1.7 and the number of attached nanorods is monitored in real-time. Once the chosen number of nanorods are permanently attached, the chamber solution can be changed. Only the nanorods with the approximate alignment of their long axis parallel to the WGM polarization direction significantly contribute to the sensing signals. For a typical optoplasmonic sensor, five gold nanorods are bound to a bare microsphere whose Q is 10^7 and are oriented approximately perpendicular to the equatorial plane of the microsphere. The resultant Q factor of the hybridized system can reach 5×10^6. Nevertheless, compared to the typical intensity enhancement factor of over 10^3, the influence of two-fold degradation of the Q factor is negligible. The other advantage of using metal nanostructures is that,

as shown in FIG. 2e, functionalizing the nanoparticle's surface with multiple receptor sites (such as antibodies) creates a label-free sensor capable of sensing specific ligand molecules such as viruses, DNA strands, proteins and even ions, considerably simplifying sample preparation. More discussion on the resonance-shift sensing mechanism can be found in Supplementary Note 5.

[H3] Mode broadening

Single nanoparticles and, in principle, molecules may be also detected by monitoring the WGM linewidth[12]. When a nanoparticle/molecule is adsorbed onto a microcavity, it opens extra dissipation channels, such as Rayleigh scattering and absorption losses, for intracavity photons, broadening the transmission spectrum (FIG. 2d). Mode-broadening-based sensing has been performed on single metal nanoparticles[111] and lentiviruses[12]. This detection method requires sufficient suppression of other broadening influences caused by, for instance, the tapered fibre coupler. To this end, a microcavity with a slightly deformed structure may be adopted so that the WGM excitation and the collection of transmitted light can be accomplished in free space with a high efficiency[112-114]. Nevertheless, the free-space excitation and detection restrict the application of deformed microcavities in aqueous environment.

[H3] Exceptional-point-enhanced sensing

In conventional mode-splitting-based sensing, a microcavity operates at a diabolic point, around which the frequencies of two or more modes coalesce into one while the modes stay orthogonal and linearly independent. The mode splitting Δ_{DP} around a diabolic point depends linearly on the strength ϵ of environmental perturbations (FIG. 3a). Recently, it has been shown that setting the operation of a WGM sensor at an exceptional point **[G]**, around which not only two or more modes but also the associated mode frequencies coalesce simultaneously (Supplementary Note 6), may enhance the sensor's sensitivity[115-118]. The mode splitting Δ_{EP} around, for example, a two-fold exceptional point scales as $\sqrt{\epsilon}$ (FIG. 3a). For a small ϵ, the optical response of a microcavity operating at an exceptional point greatly surpasses that of a microcavity operating at a diabolic point and exceeds the sensitivity limit encountered by conventional sensing schemes[115,116]. To date, the exceptional point-based enhancement has been exploited in robust single-mode lasing[119], electronic wireless sensors that rely on inductor-capacitor microresonators[120,121], nanoscale plasmonic sensing[122], microcavity-based optical sensors[118,123] and optical gyroscopes[124,125].

In experiments, the two-fold exceptional point of a WGM microcavity can be accessed by introducing Rayleigh backscattering to a pair of frequency-degenerate clockwise and counter-clockwise WGMs[118] (FIG. 3b). When a Rayleigh scatterer such as a silica nano-tip is placed close to the microcavity, clockwise and counter-clockwise WGMs are indirectly coupled via the scatterer-

induced backscattering. Yet, the microcavity still does not operate at an exceptional point since it demands asymmetric backscattering between clockwise and counter-clockwise optical waves. To this end, another Rayleigh scatterer is introduced. Adjusting the relative position between two Rayleigh scatterers leads to fully asymmetric backscattering between two WGMs. Now the sensor is ready for detecting target nanoparticles/molecules with an enhanced sensitivity $\Delta_{EP} \propto \sqrt{\epsilon}$. Higher-order exceptional points, which in principle lead to greater sensitivity, may be implemented by using a coupled cavity arrangement[123]. In addition to isolated points, a one-dimensional line/ring and a two-dimensional sheet of exceptional points, which are highly desirable for practical purposes due to unavoidable fabrication imperfections, have also been recently demonstrated[126-128].

[H2] Stand-alone WGM probes

WGM microcavities with optical gains[129] can operate either below or above the lasing threshold **[G]**. Below the threshold, the emission spectrum of fluorescent molecules located inside a microcavity consists of sharp peaks superimposed onto the fluorescent background. Above the threshold, only a few modes within the maximum gain region typically start lasing. Semiconductor disc lasers exhibit a broad fluorescence with no sharp spectral peaks below the threshold, while only one mode starts lasing above the threshold[23]. Advantages of the lasing operation include enhanced signal-to-noise ratio, nonlinear behaviour as a function of the pump power, and high sensitivity to the change in gain medium.

For applications in cells and deep tissues *in vivo*, WGM microcavities are typically not optimized to achieve the highest possible Q factor but instead optimized to minimize their size and make them functional and biocompatible. A variety of transparent materials can be used to fabricate microcavities, including polymers[22,130], natural materials[131-133], glass and semiconductors[23,134]. Some dye-doped polymer and glass beads are also available commercially. Polymer beads may be prepared through, for example, dispersion polymerization and emulsion solvent diffusion, while microdroplets are usually prepared from a water insoluble fluid by dispersing/injecting it into water. In some situations, natural lipid droplets in live adipocytes are also employed directly. For fluorescent materials inside microcavities, almost all organic fluorescent dye (including natural materials, such as vitamin B2[135] and chlorophyll[136]), quantum dots, fluorescent proteins[137], and upconverting nanoparticles[138] can be used.

The smallest achievable size of a microcavity is limited by the refractive index and the desired Q factor. For sensing in the nonlasing regime, the Q factor can be low[139] and there is no benefit in increasing it beyond the spectrometer resolution. In contrast, as a rule of thumb to achieve laser emission by using an organic dye as gain medium, the microcavity Q factor should be on the order of 10^4. The minimum diameter of a WGM cavity to achieve such a Q factor in water at a wavelength of

550 nm is 24 μm for oil/lipid droplets (refractive index of 1.47), 11 μm for polystyrene (refractive index of 1.59), and 2.3 μm for $BaTiO_3$ (refractive index of 2). The size of semiconductor disc lasers (refractive index of 4) may be as small as 0.7 μm[134].

WGM probes can be inserted inside biological materials and organisms. Solid microcavities are internalized by mammalian cells through phagocytosis[140] while liquid droplets are injected by a micropipette[20]. Microcavities may also be injected into various tissues, such as below the skin[130] and muscle tissues[21], and operate inside body fluids such as blood[130,141,142].

Far-field fluorescent excitation and detection must be implemented for live cell and *in vivo* applications because evanescent coupling is impractical inevitably degrading sensitivity. In addition, the small microcavity size leads to a low Q factor and there are other noise sources within live organisms that further limit sensitivity. The fluorescently labelled microcavities are usually pumped by using the standard equipment that is normally applied for fluorescent imaging. The lasing action is driven by a nanosecond or picosecond pulsed laser with an energy of pJ ~ a few nJ and a repetition rate ranging from Hz to several kHz. The signal from a single microcavity may be attained using the point illumination of a focussed laser and/or point detection through a pinhole to enable confocal detection. Imaging several microcavities requires one to move the excitation/detection spot across the sample, yielding a hyperspectral image[20,23].

[H2] Microring resonator-based sensing

[H3] Evanescent field sensing in microring resonators.

Chip-integrated, silicon photonic microrings have emerged as the most promising WGM sensing format due to advantages in scalability, multiplexing potential, and standardized fabrication[143], and have been commercialized by Genalyte, Inc. (FIG. 4a)[144,145]. An additional advantage of these microrings is the ability to easily optically interrogate sensors using chip-integrated grating couplers to access waveguides **[G]** adjacent to the microrings. Light propagates through linear waveguides under total internal reflection and wavelengths that satisfy the resonance condition couple into the microring[146,147]. Since the evanescent field is sensitive to local changes in the refractive index of the exposed cavity, the resonance wavelength shifts in response to biomolecular binding-induced changes in refractive index[148,149]. The commercial system enables the resonance wavelength of each ring on the chip to be read out quickly by rastering the laser across different input grating couplers[144,145]. One key element of these chips is that thermal control rings, which are covered by an inert cladding material and unexposed to the sensing solution, allow for correction of resonance drifts due to temperature fluctuations[150]. An additional consideration in constructing sensor arrays is the size of individual sensing elements, particularly when considering multiplexed detection applications. While microrings can be fabricated to very small diameters, the key limitation for many

applications is the ability to selectively deposit different analyte-specific capture agents onto the sensor array (FIG. 4b).

[H3] Biomarker detection on microring resonators.

In order to detect specific biomarkers of interest, microring resonators must be modified with analyte-specific capture agents. These can include antibodies[145,151], antibody fragments[152], complementary nucleic acid aptamers[19] or other specialized recognition molecules. Most microring resonators are constructed of materials that can be functionalized using straightforward silane and bioconjugate chemistries[153-155]. Microring resonators have been used for label-free detection of targets including nucleic acids[18,19], viruses[156], proteins[145,151], nanodiscs[157], and telomerase activity[158]. The principle of label-free sensing relies on a highly specific capture agent pulling down the biomarker into the sensing region to result in a resonant wavelength shift.

As an alternative to label-free detection, additional assay reagents may be incorporated to increase the per-analyte refractive index change. Such reagents include secondary (tracer) antibodies[159,160] and (sub-)micron-scale beads[161,162]. In addition, secondary reagents can include enzymatic tags that can create extremely large per-analyte resonance shifts and allow sub-pg/mL limits of detection for proteins[163,164]. This signal amplification closely resembles the current gold standard assay for protein quantitation (a sandwich-style enzyme-linked immunoassay), where a pendant enzyme can convert a soluble reagent into an insoluble precipitate that is deposited at the microring surface leading to extremely large resonance wavelength shifts that are tracked over the course of the varying binding events[165,166] (FIG. 4c). An example of this immunoassay is depicted in FIG. 4d, where sensor arrays modified with analyte-specific antibody capture agents localize the target molecule to the microring surface. A secondary recognition element (typically a tracer antibody) that has a biochemical handle for subsequent recognition is then introduced. Importantly, this second antibody provides high specificity for the targeted analyte because two high affinity interactions are now localized near the microring surface. The secondary element can then be additionally recognized by a tertiary reagent, such as a streptavidin biomolecule linked to an enzyme. Finally, enzymatic processing of solution-phase chemicals gives an extremely large resonance shift that is proportional to the amount of target analyte in the initial sample solution, depicted as step 4 in FIG. 4c, d. While requiring multiple assay steps, these assays have been shown to decrease limits of detection, provide clinically relevant dynamic ranges and greatly improve assay specificity[161,167].

[H2] Optomechanics

In addition to optical WGMs, microcavities also host mechanical modes that are parametrically coupled with optical degrees of freedom via the radiation pressure force. Accessing weak radiation pressure effects has two prerequisites: large intracavity light power and long photon lifetime. Large enough intracavity light power provides a sufficient radiation pressure force, where the amount of power of a circulating beam is $\mathcal{F}/\pi$ times as large as that of the launched input beam. The highest reported finesse $\mathcal{F}$ for a WGM microcavity reached 2.2×10^6 (REF.[8]), exceeding that of Fabry–Pérot cavities[168-170]. Long photon lifetime, comparable to or ideally surpassing the mechanical oscillation period, ensures the observation of dynamical effects of the optomechanical coupling.

[H3] Mechanism

To understand the underlying mechanism of optomechanics, let us first consider a simple case, where an optical Fabry–Pérot cavity contains a movable mirror that experiences a small one-dimensional displacement $x(t)$ from its initial position (FIG. 5a). In the linear approximation, the cavity mode frequency is given by $\omega_0 + \xi x(t)$ with the component ω_0 in the absence of the displacement, the optomechanical coupling constant $\xi = -\omega_0/L$, and the cavity length L. Input light E_{in} at frequency ω_1 pumps the cavity with an incident photon flux $P_{\mathrm{in}} \equiv |E_{\mathrm{in}}|^2$. The displacement $x(t)$ undergoes a damped harmonic motion with a radio oscillation frequency Ω and a damping rate Γ. The modulated light field $E(t)$ inside the cavity consists of two sidebands at $\omega_1 + \Omega$ and $\omega_1 - \Omega$ around the central component at ω_1. The radiation pressure $F(t) = -\hbar\xi|E(t)|^2$ that results from reflecting the intracavity photon flux is exerted on the movable mirror. The radiation pressure is, in general, tiny but it may still cause the deformation of micron-sized objects, for example, aqueous droplets. Such a deformation can be observed through optical microscopy[171]. The steady state of the optomechanical system depends strongly on the input light (Supplementary Note 7). The above analysis is applicable to WGM microcavities by replacing the cavity length L with the microcavity's radius R (FIG. 5a). The circulating photons exert a radial radiation pressure on the microcavity and induce a structural deformation (Supplementary Note 8).

[H3] Ultrasensitive motion transduction

We now come to the question of how to detect the small displacement $x(t)$. Changes in Fabry–Pérot cavity length or the WGM microcavity's radius shift the mode resonance frequency, thereby imprinting the mechanical motion $x(t)$ onto the optical phase $\varphi(t)$ with an enhancement factor $\mathcal{F}/\pi$ (FIG. 5b). The modulated phase $\varphi(t)$ may be read out by comparing the transmitted probe light from the cavity to an optical reference and the noise spectral density **[G]** $\bar{S}_{xx}(\omega)$ of $x(t)$ is derived. The minimum detectable displacement δx_{min} is then given by $\delta x_{\mathrm{min}}/\sqrt{B} = \sqrt{\bar{S}_{xx}(\omega)/4}$ with a

measurement bandwidth B. Three main noise sources that are the quantum shot noise **[G]** of counting photons[28] with a spectral density $\bar{S}_{xx}^{\mathrm{imp}}(\omega)$, the quantum fluctuation of the radiation pressure force with a spectral density $\bar{S}_{FF}(\omega)$, and the thermal Langevin force with a spectral density $\bar{S}_{FF}^{\mathrm{th}}(\omega)$ contribute to $\bar{S}_{xx}(\omega) = \bar{S}_{xx}^{\mathrm{imp}}(\omega) + |\chi(\omega)|^2\left[\bar{S}_{FF}(\omega) + \bar{S}_{FF}^{\mathrm{th}}(\omega)\right]$, where $\chi(\omega)$ denotes the susceptibility **[G]** of the mechanical oscillator. An efficient way to suppress the shot noise is to use squeezed probe light[172,173]. The spectral densities $\bar{S}_{xx}^{\mathrm{imp}}(\omega)$ and $\bar{S}_{FF}(\omega)$ satisfy the fundamental Heisenberg uncertainty **[G]** relation[174] $\bar{S}_{xx}^{\mathrm{imp}}(\omega)\bar{S}_{FF}(\omega) > \hbar^2/4$. The thermal Langevin force may greatly exceed the radiation pressure force noise at room temperature. When the mechanical oscillation frequency Ω greatly exceeds the damping rate Γ, $|\chi(\omega)|$ peaks at Ω and $\bar{S}_{xx}(\Omega)$ is of interest. Figure 5c illustrates the dependence of $\bar{S}_{xx}(\Omega)$ on the input power P_{in}. At zero environmental temperature, $\bar{S}_{xx}(\Omega)$ reaches its minimum $\bar{S}_{xx}^{\mathrm{SQL}}(\Omega)$, which is referred to as the standard quantum limit, under the optimum measurement condition $\bar{S}_{xx}^{\mathrm{imp}}(\Omega) = |\chi(\Omega)|^2\bar{S}_{FF}(\Omega)$.

In experiments, the shot-noise-limited optical phase measurement, $\bar{S}_{xx}(\omega) \approx \bar{S}_{xx}^{\mathrm{imp}}(\omega)$ may be easily implemented via balanced homodyne detection **[G]** [175]. The measurement of the Brownian motion of a Fabry–Pérot-type optical cavity has been shown to have a sensitivity $\delta x_{\mathrm{min}}/\sqrt{B}$ of 10^{-20}~10^{-19} m Hz$^{-1/2}$ [176,177]. For a silica WGM microcavity with typical parameters $\mathcal{F} = 5 \times 10^4$, $P_{\mathrm{in}} = 1$ μW, and $\omega_0 = 2\pi \times 282$ THz, the shot-noise-limited displacement can be, in principle, as small as $\delta x_{\mathrm{min}}/\sqrt{B} = 5 \times 10^{-19}$ m Hz$^{-1/2}$. Yet, a practical displacement measurement has not reached this level because of the excess phase noise in the probe laser. Recent WGM optomechanical experiments[34,178] have achieved a transduction sensitivity of 1.5×10^{-18} m Hz$^{-1/2}$. Other optical phase measurement techniques include the Hänsch–Couillaud approach based on polarization spectroscopy[35,179] and the Pound–Drever–Hall method based on frequency modulation spectroscopy[180-182].

[H3] Optomechanical single-molecule sensing

Optomechanical coupling can also be used to detect single molecules. Let us consider a blue-detuned pump laser at ω_1 exciting a mechanical mode at Ω. Any small fluctuation $\delta\omega$ to the microcavity resonance frequency ω_0 is transferred to the frequency shift $\delta\Omega = [d\Omega/d(\omega_1 - \omega_0)]\delta\omega$ of the mechanical mode. The minimal detectable $\delta\Omega$ is determined by the linewidth Γ of the mechanical mode. Thus, the optical single-molecule sensitivity is limited by $|\delta\lambda/\lambda_0|_{\mathrm{min}} = |\delta\omega/\omega_0|_{\mathrm{min}} = 1/\eta Q_{\mathrm{m}} Q$ with the transduction factor $\eta = (\kappa/\Omega)|d\Omega/d(\omega_1 - \omega_0)|$ and the quality factor $Q_{\mathrm{m}} \equiv \Omega/\Gamma$ of the mechanical mode. Substituting the experimental values $\lambda_0 = 974$ nm, $Q = 2.6 \times 10^6$ (in water), $\Omega = 2\pi \times 262$ kHz, and $d\Omega/d(\omega_1 - \omega_0) = 7.6 \times 10^{-4}$, one has $\eta = 2.1$ and thus the sensing resolution is approximately enhanced by the Q_{m} factor of the

mechanical mode compared to conventional approaches. Such a cavity optomechanical spring sensor has been demonstrated[183], where the radial breathing mechanical mode[184] (Supplementary Note 8) in a microsphere detected single bovine serum albumin proteins in an aqueous environment with a sensitivity $|\delta\lambda/\lambda_0| = 1.5 \times 10^{-10}$.

[H1] Results

Single-molecule sensors are at the cutting edge of biochemical sensing. Here, we highlight single-molecule sensing results to general readers[42]. To date, biosensing at the single-particle level has been achieved for dielectric nanoparticles, viruses, DNA, proteins and atomic ions (TABLE 1). Detecting dielectric nanoparticles usually illustrates a sensing mechanism while the sensing of biomolecules directly demonstrates practical applications. Single molecules are studied on optoplasmonic biosensors[14,101], the most sensitive WGM-microcavity-based devices, where the localized surface plasmon resonance of metal nanoparticles enhances the evanescent field of a WGM microcavity (FIG. 3c). These biosensors employ the mechanism of mode resonance shift and usually operate in an aqueous environment. FIG. 3e shows that the surface of metal nanoparticles is functionalized by receptor molecules (A) that primarily interact with specific ligand (B) molecules in solutions, leading to a label-free monitoring of the biochemical reaction in real-time such that:

$$\mathrm{A} + \mathrm{B} \underset{k_{\mathrm{off}}}{\overset{k_{\mathrm{on}}}{\rightleftharpoons}} \mathrm{AB}, \quad (3)$$

Here, the on-rate constant k_{on} (in units of $\mathrm{M^{-1}\,s^{-1}}$ with 1 M = 1 mol/L) measures the rate of the ligand binding to the receptor and the off-rate constant k_{off} (in units of $\mathrm{s^{-1}}$) denotes the rate of the ligand dissociating from the receptor. In equilibrium, forward binding and backward unbinding processes reach the balance $k_{\mathrm{on}} c_{\mathrm{A}} c_{\mathrm{B}} = k_{\mathrm{off}} c_{\mathrm{AB}}$ where, for example, c_{AB} represents the concentration of the product AB.

[H2] Spike-events

The perturbations of the bimolecular reaction between ligands and receptors on the WGM resonance wavelength λ_0 have two types, spike and step events[14,101]. When a ligand molecule approaches a receptor site on a gold nanorod, λ_0 experiences a red shift. Subsequently, λ_0 undergoes a blue shift when the ligand dissociates from the receptor, leaving a spike pattern in the trace of the resonance wavelength λ_0 (FIG. 6a). Each spike is characterized by a height $\Delta\lambda$, which depends on where the transient single-molecule event occurs, and a duration τ that measures the binding interaction time. Only the spikes whose $\Delta\lambda$ and τ respectively exceed the background noise floor (FIG. 6b) and the sensor's time resolution can be detected. Experimental observations[14,101] show that the duration τ follows an exponential distribution with an average duration τ_{ave} (FIG. 6c).

τ_{ave} is directly linked to the kinetic off-rate $k_{off} = \tau_{ave}^{-1}$, which allows one to evaluate k_{off} from measuring τ_{ave}. For instance, experiments[185] show that $k_{off} = 20{\sim}70$ s^{-1} for polymerases interacting with DNA strands depending on specific polymerase species, temperature, and the absence/presence of deoxynucleoside triphosphate. In addition, the statistics of transient receptor-ligand binding **[G]** events matches the Poisson distribution. That is, the probability of $K \in \mathbb{Z}$ spikes (where $\mathbb{Z}$ denotes integers) occurring in a resonance wavelength trace with a time length Δt takes the form $p(K, \Delta t) = (R_b \Delta t)^K e^{-R_b \Delta t}/K!$. Here, $R_b = \sum_{j=1}^{N_A} r_j$ accounts for the total binding event rate (in units of s^{-1}) with the rate r_j corresponding to the jth receptor site and the number N_A of receptor sites. Setting Δt as the interval between two adjacent spike events, one arrives at $p(K = 0, \Delta t) = e^{-R_b \Delta t}$, that is, the statistics of Δt satisfies an exponential distribution with an average constant equal to R_b^{-1} (FIG. 6d). The total event rate R_b grows linearly with the ligand concentration c_B[101] and the kinetic on-rate constant is then given by $k_{on} = R_b/N_A c_B$ (FIG. 6e). The rate k_{on} cannot be evaluated without the knowledge of N_A. When $R_b \tau_{ave} < 1$, single-molecule events predominate in receptor-ligand interactions. In contrast, two receptor-ligand interaction events overlap with each other when $R_b \tau_{ave} > 1$ and thus cannot be distinguished.

[H2] Step events

A step event occurs when a ligand permanently binds to a receptor (FIG. 6f). The resultant step shift $\Delta\lambda$ of the resonance wavelength is a positive shift for each of the detectable single-molecule binding events. For single-nanoparticle detection, $\Delta\lambda$ can be either positive or negative[43] (FIG. 6g) because of the interference between backscattering lights[99]. The interval Δt between adjacent step events still follows an exponential distribution (FIG. 6h). In addition to the WGM resonance shift, single-molecule events can be also revealed by tracking the extra broadening $\Delta\kappa$ of the WGM linewidth (FIG. 6i). However, the occurrence of step broadening events does not always coincide with step resonance shift events. The value of $\Delta\kappa$ may be either positive or negative (i.e. narrowing the WGM linewidth)[107,186] (FIG. 6j), which again is ascribed to the backscattering interference between different nanorods[99], and is not proportional to $\Delta\lambda$. Since permanent binding interactions consume the receptor sites on nanorods, the cumulative count of step resonance shift events becomes saturated after a long period (FIG. 6k). In addition, the occurrence of a spike or a step event depends on the receptor-ligand interaction strength. For example, the interaction between two mismatched oligonucleotide strands tends to cause a spike event while a step event more likely occurs for the interaction between two matched oligonucleotide strands[14]. Changing aqueous environmental factors, such as NaCl concentration[14], temperature, solution's pH[107], and the reducing agent[106] may adjust the receptor-ligand interaction, leading to a transition between spike and step events. More

complex signal shapes arise in studies of the conformational changes of proteins such as for active enzymes immobilised on optoplasmonic sensors[106]. More discussion on environmental factors affecting spike and step events can be found in Supplementary Note 9. The methods of quantifying biomarkers detected on the WGM sensors are discussed in Supplementary Note 10.

[H1] Applications

In addition to sensing, WGM microcavities have various other applications. Due to their small mode volumes and ultrahigh Q factors, WGM microcavities are an outstanding platform for engineering laser emission[27] with wavelength spanning from ultraviolet to infrared. These micro-sized lasers may operate as light sources in photonic integrated circuits[33] and are of particular importance in quantum information processing and computing[187]. In addition, WGM microcavities have been extensively used in exploring nonlinear optical behaviours such as electromagnetically induced transparency[188-190] and nonlinear optical frequency conversion[173,191-193]. Moreover, WGM-microcavity-based optical frequency combs[193-195] are particularly useful in on-chip optical frequency metrology and precision measurement. In this section, we only present selected examples of WGM-microcavity-based applications in sensing and physics. Other applications in, for examples, trapping and manipulating single particles, cooling mechanical fluctuations, electromagnetically induced transparency and frequency microcombs, can be found in Supplementary Note 11 where relevant references are provided for interested readers.

[H2] Biosensing

Biosensing based on WGM microspheres and microtoroids has been performed on proteins (bovine serum albumin and the binding interaction between streptavidin and biotinylated bovine serum albumin[11]), DNA[196], viruses (lentiviruses[12] and influenza A virions[100]), and cells (exosomes[197] and interleukin-2 [198]). The relatively large polarizabilities of these biomolecules allow for sensing detection at the single-molecule level[12,100,183] exclusively using microcavities. Detecting single dielectric nanoparticles (such as potassium chloride and polystyrene) is also typically performed to elucidate sensing mechanisms. Hybridizing solid WGM microcavities with metal nanoparticles enables the detection of molecules with very small polarizabilities, for example short single-stranded nucleic acids[14], biotinylated poly(ethylene glycol)[104], and even atomic ions[101]. Label-free sensors enable monitoring single-molecule biochemical reactions in real-time[104,107].

In *in vivo* sensing applications, the absolute size of the microcavity and the refractive index of its surrounding medium can be extracted independently by analysing both TE- and TM-polarized modes[199,200]. Further, the microcavity or the coating can be made from a responsive material whose properties (such as volume, refractive index, fluorescence, etc.) change upon some external factors

(for examples, humidity, temperature, pH, etc.). These changes occur due to various mechanisms such as swelling[201], structural changes in the material[133], reorientation of the molecules at the surface[202], and change in the fluorescent intensity due to the Förster resonance **[G]** energy transfer[203] or binding of a fluorescent dye[142]. Despite the great sensitivity of WGM microcavities, the adsorption of molecules to a microcavity has not yet been demonstrated inside cells or tissues.

WGM microcavities in the form of liquid droplets and soft solid beads have great potential to measure the force and strain within cells and tissues. When a droplet is deformed, the WGM spectrum presents a broadening or splitting, allowing for a precise measurement of the deformation[20,204]. The force and strain may be evaluated by analysing the deformation and mechanical properties of the microcavity. Soft droplets are used to measure tiny forces within cells[20] while solid spheres are used for large forces and stiffer tissues[204]. In most traditional force measurement techniques, the cells are placed in contact with an artificial material while WGM-based force transducers can be placed inside tissues without much perturbation. Compared to molecular tension sensors[205], WGM-based transducers have other advantages such as force direction measurement, large dynamic range, and insensitivity to the environmental factors.

An important application of WGM probes is their use as optical barcodes for cell tagging and tracking[22-24]. Thousands of unique emission spectra can be generated by differently-sized microcavities that are optionally combined with several different fluorescent media. The spectrum itself and the microcavity's size calculated from the spectrum can be employed as the identifier. Purely spectral barcodes offer several advantages, including noncontact readout that does not require optical imaging to read the barcode. A single WGM microcavity may work as a multimode probe to simultaneously perform sensing and tracking and possibly as a light source for imaging[206,207]. Furthermore, since the spectral positions of the emitted narrow lines do not move when propagating through a scattering medium, the microcavities can also operate within deep tissues such as inside the skin[130]. Both barcoding and sensing can be performed for time-dependent refractive index measurement[21].

[H2] Gyroscopes

Optical gyroscopes, making use of laser Sagnac interference **[G]**, are essential to aeronautics, navigation and positioning. A conventional Sagnac ring interferometer rotates in its plane at an angular velocity, yielding a round-trip phase difference between a pair of degenerate counter-rotating light waves. This extra phase difference lifts the mode degeneracy and leads to a frequency splitting in the spectrum. The first laser gyroscope was reported in 1963 (REF.[208]). Miniaturizing optical gyroscopes has been a long-term pursuit in many industrial applications. However, the small area of the Sagnac loop **[G]** requires exceptionally stable cavity modes for the measurement of tiny

phase differences. Due to the recent development of low-loss fibres/waveguides and chip-based WGM microcavities with ultrahigh Q factors, building a compact and robust optical gyroscope sensor is promising. For a passive WGM-based gyroscope[209] where a pair of degenerate clockwise and counter-clockwise WGMs are pumped by a probe laser, its angle random walk **[G]** and bias drift **[G]** can be as small as 0.02 deg $h^{-1/2}$ and 3 deg h^{-1} respectively. These are over one order of magnitude better than those based on waveguide ring resonators[210-212]. This allows for the detection of an optical path change of 1.3×10^{-16} cm, three orders of magnitude smaller than the classical electron radius of 2.8×10^{-13}. In contrast, an active WGM-based gyroscope may be implemented by employing two nondegenerate clockwise and counter-clockwise lasing modes with Brillouin gain[213]. Such a Brillouin gyroscope has been used to measure the earth's rotation[214] with an angle random walk 0.068 deg $h^{-1/2}$ and a bias drift of 3.6 deg h^{-1}.

[H2] Parity-time symmetric optics

One of fundamental postulates of quantum mechanics says that the reality of physical observables relies on the Hermiticity **[G]** of associated operators. However, it has recently been pointed out that the eigenvalues of a non-Hermitian Hamiltonian can be all real when the Hamiltonian satisfies the invariance under the combination of parity and time-reversal operations[215]. Owing to their excellent flexibility and controllability, gain-loss-balanced optical systems provide a versatile platform for exploring the fundamental nature of non-Hermitian parity-time-symmetric physics. The simplest system is composed of two coupled optical cavities, where one cavity experiences an optical gain while the other suffers from photon loss. When the intercavity coupling strength is larger than the optical gain/loss coefficient, the coupled system is in the unbroken phase, where the eigenfrequencies of two cavity modes are both real (Supplementary Note 11). The power of either intracavity field exhibits an oscillatory behaviour and the total power of two intracavity fields also oscillates. In contrast, when the intercavity coupling strength is smaller than the optical gain/loss coefficient, two eigenfrequencies become complex conjugate to each other and the coupled system is in the broken phase, where one intracavity field increases exponentially while the other decays exponentially. The transition from the unbroken phase to the broken phase is referred to as spontaneous parity-time symmetry breaking.

The parity-time-symmetric optical system **[G]** was first carried out passively with an asymmetric low-loss-high-loss-type optical potential[216]. Later, a coupled system with an asymmetric gain-loss profile was implemented by using a pair of waveguides on a Fe-doped lithium niobate substrate[36]. WGM microcavities have also been widely used to unveil distinct features, for example nonreciprocity **[G]** , in parity-time-symmetric optics. The forward and backward transmission spectra of a pair of coupled microtoroids with balanced optical gain and loss have been shown to have a

similar profile when the system is in the unbroken phase, whereas the transmission becomes unidirectional in the broken phase[37]. The parity-time symmetry also strongly affects lasing dynamics. A pair of coupled active and passive microcavities in the broken phase suppress competing parasitic modes and enforce the stable single-mode operation[119]. The conventional formulation of parity-time-symmetric optics is mainly based on the adiabatic elimination of medium polarization, which becomes invalid in the strong light-matter interaction regime, where distinct phenomena emerge[217].

[H2] Microcavity QED

Cavity QED explores the interaction between an atomic dipole and a single-mode optical cavity (FIG. 7a), where the quantum nature of light plays a notable role. The two-level atom is composed of a lower $|\downarrow\rangle$ state and an upper $|\uparrow\rangle$ state with a transition frequency ω_{at} that is near resonant to the cavity mode frequency ω_0 and has an electric dipole moment d. The energy dissipation sources in the system include the spontaneous emission of the atom from $|\uparrow\rangle$ to $|\downarrow\rangle$ at a rate γ and the intracavity photons escaping from the cavity at a rate κ. When the atom-cavity coupling strength $g = d\sqrt{\omega_0/2\varepsilon_0\hbar V_{\text{eff}}}$ is much larger than both γ and κ in the strong-coupling regime, the quantum behaviours of the coherent atom-photon interaction, such as an avoided level crossing in the transmission spectrum of the optical cavity (FIG. 7b), appear well before the dissipation sources take effect (Supplementary Note 12). Cavity-QED systems are of great interest in the study of fundamental quantum effects in light-matter interactions, for examples, vacuum Rabi splitting[218] **[G]**, enhanced spontaneous emission of atoms[219], quantum jumps of intracavity photons[220] and various other applications, for instance one-atom lasers with nonclassical properties[221], quantum logic gates in quantum computing[222] and quantum information processing[223].

A small V_{eff} boosts the atom-cavity coupling, and WGM microcavities are in principle an excellent cavity-QED platform[40]. A recent experiment has demonstrated the strong evanescent coupling between individual caesium atoms and a silica microtoroid ($\kappa = 2\pi \times 17.9$ MHz)[31]. The WGM frequency ω_0 is near resonant to the caesium D2 line ($\gamma = 2\pi \times 5.2$ MHz) at $\lambda_{\text{at}} = 852$ nm. In the absence of atoms, the microtoroid operates at the critical fibre-microcavity coupling condition. The strong atom-cavity interaction destroys this condition and gives rise to an increase in the forward propagating power in the fibre. The experimental result shows an atom-cavity coupling strength $g = 2\pi \times 70$ MHz, greatly larger than κ and γ, and a Purcell factor $F_{\text{P}} = 200$. Nevertheless, the short atom-transit time (~ 1 μs) seriously restricts the atom-microcavity interaction time. In addition, for atoms positioned on a sub-wavelength scale near the microcavity's surface, the large radiative atom-microcavity interaction strongly affects the atom's dynamics[224].

Trapping atoms in the vicinity of a WGM microcavity is an efficient way to extend the atom-microcavity interaction time (FIG. 7c). A few theoretical studies[225,226] have proposed an atom gallery,

in which three-level V-type atoms interact with two oppositely detuned WGMs. A more promising approach is using two-colour evanescent optical trapping[227], where the red-detuned optical potential attracts atoms towards the microcavity's surface while the blue-detuned optical potential pushes atoms away from the microcavity's surface. Combining these with the attractive van der Waals potential, a three-dimensional potential well may be formed at a distance of a few hundred nanometers from the microcavity's surface[41,228] (FIG. 7d).

[H1] Reproducibility and data deposition

The field of WGM sensors is diverse; reproducibility is typically determined in individual laboratories, and there is not a specific type of data generated that lends itself to a repository. However, the resulting measured quantities such as protein concentrations can be compared against alternative detection strategies.

Device fabrication can be difficult for WGM sensors, though notable exceptions are surface-nanoscale-axial-photonics microresonators with sub-angstrom precision[94,229,230], silicon-on-insulator microrings, and an interesting approach to batch fabricating microtoroidal resonators[231]. High performance resonators necessitate exact lithography and etching in many cases to ensure smooth and reproducible geometries that support high Q factors, and this was one of the first methods that demonstrated reproducible, batch fabrication of many high Q resonators on a single chip. While robust methods exist to batch fabricate lower Q factor microrings, the creation of high Q microtoroids at chip scale was an important development for the field. In addition, device geometries that rely upon a freestanding optical fibre for interrogation have the additional difficulty of aligning coupling fibres with high reproducibility.

To limit sample handling and improve reproducibility, WGM sensors can be integrated with a microfluidic system. The recent developments in lab-on-a-chip microfluidic platforms have built upon the benefits of increasing consistency or sensing results, automation of assays, and decrease of reagent consumption and time to result[231]. Microfluidic integration varies across WGM sensor types. For small chip-based sensors, microfluidic channels can be fabricated to flow across the sensor surface such as in a two-channel design with polydimethylsiloxane[232]. For hollow resonators, the sensor can be packaged together with sensing components (such as the fibre) and microfluidic ports to pump liquid through the resonator in a controlled and confined manner[231,233]. For *in vivo* sensors, bio-integrated cavities usually interrogate only their immediate vicinity; combined with the biological system's heterogeneity and dynamic behaviour, this may cause large variations in measurements. This can be an advantage when we are interested in local properties, for example cell-to-cell variation, but to measure overall properties of an organism, more measurements averaged over space and time are required to get sufficient statistics.

Currently, there is no general repository for WGM biosensor data. The data collection and analysis vary sensor to sensor and application to application, making a general repository unnecessary. However, as the field of WGM sensing grows, it would be conceivable to create a repository for specific types of sensors (such as microrings, microtoroids, microbubbles) or for specific applications (such as biomarker detection or nucleic acid detection). For newly developed sensors, the fundamental characteristics including Q factor and dimensions and fabrication specifications should be reported. In application focused work, analytical measures of limits of detection, limits of quantification, and linear dynamic ranges for each analyte of interest should be reported, which are dependent on the properties of the reagents and not necessarily on the sensor itself. For reports of biomarker quantitation, the calibration equation used for that application should be reported.

[H1] Limitations and optimizations

Various environmental, technical/methodological and instrumental factors limit the detection sensitivity. Some of them may be potentially bypassed through employing different measurement methods while substantial efforts are needed to overcome others.

[H2] Time resolution of biochemical sensing

For conventional transmission-spectrum-based biosensing, the probe laser wavelength is continuously swept over the WGM central wavelength with a range wider than the mode linewidth. To accurately capture the entire transmission spectrum of a sensor, the sweeping rate must be slow enough that the intracavity field continuously maintains a steady state. The frequency shift, mode splitting, and extra spectral broadening are evaluated by real-time fitting. Consequently, the time resolution for the single-molecule detection is usually limited to tens of milliseconds[14,101]. One way to address this issue is to lock the probe laser frequency to the microcavity. As demonstrated in REFS[197,198], the sampling (detection) time can be as short as 0.05 ms, significantly improving the time resolution. Another potential way is using cavity ring-up spectroscopy[234,235], where the microcavity is pumped by a sequence of far-detuned light pulses and single-molecule events are identified by measuring the beat note between the probe beam and the microcavity output field (see Supplementary Note 5). This technique may allow for monitoring biochemical reaction kinetics at nanosecond timescales, orders of magnitude faster than traditional detection methods.

[H2] Hollow WGM resonators

One of the main limitations for the achieved sensitivity of hollow WGM resonators is related to the material absorption leading to a reduction in the overall Q factor. For quasi-droplets, the loss due to

the absorption by the microcavity's material is negligible compared to that of the contained fluid. However, quasi-droplets have the clear advantage that the sensing region is impervious to several environmental factor, such as air flow, dust contamination and rapid fluid evaporation (Supplementary Note 5). For nonlinear optics applications, dispersion engineering relies on a well-controlled fabrication method to ensure that a desired resonator radius and wall thickness can be achieved. Improved fabrication techniques, ensuring a geometric repeatability similar to what can be achieved for wafer-scale processing of microdisks and microtoroids, are highly desirable.

[H2] In vivo sensing

Before using microcavities in live organisms, the potential negative effects must be considered. The microcavities need to be made from or coated with biocompatible materials or possibly made biodegradable. Even if the particle is made of a biocompatible material, the microcavity's size alone can alter the biological processes. Several studies of the internalization of large particles (up to 20 µm) into cells did not find any significant effect on cell viability when studying the cells up to 10 days[140,236,237]. However, more subtle effects can be present. The use of microcavities potentially causes an immune response, which may lead to inflammation and foreign body response. Phototoxicity also needs to be considered. However, the fluorescent material is usually contained within the cavity that interacts with the biological environment with a rather small surface area.

Inside a live organism, the dynamic biological environment is the main contribution to the noise, thereby limiting sensitivity. Thermal and active movement of cellular organelles, cell movement and division, blood flow, muscle movement and changes in concentration of solutes can change local refractive index and induce random shifts in the wavelength. For example, the wavelength shift for a cavity inside a non-dividing live cell in a stable environment can be as large as 0.1 nm within a few minutes.

[H2] Analytical noise considerations

There are three major sources of measurement noise when dealing with WGM sensors[167]. The first is the noise associated with non-optimized optical coupling from the interrogation waveguide into the resonator, though this can be solved through clever engineering, for example by physically anchoring the linear waveguide onto the resonator-containing chip. Another significant potential source of noise is thermal fluctuation. The materials of the resonator and surrounding environment have different thermo-optical coefficients. Thus, their refractive indices do not move in unison when the temperature across the chip varies even by very small amounts. For this reason, the integration of thermal control sensors that are unresponsive to (bio)chemical binding yet are exposed to the same temperature fluctuations are critically important. Temperature variance even at the level of 10^{-3} °C

773 can lead to enormous resonance shifts that dwarf those observed by chemical or biomolecular
774 binding events. Finally, the most challenging source of noise for biosensing is biological. When
775 flowing solutions containing biomolecular targets of interest, other biochemicals are present and
776 produce an inherent background of resonance wavelength fluctuations due to either bulk refractive
777 index changes or non-specifically bound molecules. Furthermore, the levels of these non-specific
778 responses can vary widely among samples, particularly patient-derived samples. Therefore, in many
779 practical applications, the ability to determine resonance wavelength shifts is limited by "non-
780 optical" noise, for example, thermal and biological noise, rather than by optical performance, which
781 means that higher Q factors, while theoretically providing better sensitivity, often do not yield
782 enhanced performance for biological assays. Resolving and reducing the limiting noise becomes less
783 of an analytical sensor development task and more of an assay characterization endeavour, such as
784 preferentially selecting high affinity reagents and decreasing non-specific interactions of biological
785 components on the sensor surface.
786
787 ## [H2] Multiplexing
788 An inherent advantage of microscale sensors of any type is the ability to integrate many sensors into
789 a small footprint. This enables potential multiplexing to detect multiple target analytes
790 simultaneously. To this end, microrings and microdisks appear to be the most promising for
791 multiplexing, due to their planar geometry that simplifies fabrication[238], while also making them
792 amenable to microspotting **[G]** of capture agents onto different sensor elements on the same chip[25].
793 To optimize a multiplexed assay, each target on the sensor should be optimized individually,
794 followed by cross-reactivity measurements that ensures only the sensors functionalized with the
795 capture probe for a particular biomarker increase in signal in the presence of that specific
796 biomarker[239]. This process must be repeated for every target in the multiplexed system to check that
797 the results are due to the presence of the analyte in samples and not due to non-specific adsorption
798 or other aberrant responses.
799
800 ## [H2] Non-specific adsorption considerations
801 Non-specific adsorption refers to the adhesion of non-targeted proteins to the surface of the sensor
802 regardless of surface functionalization. This can cause resonance shifts and lead to a false positive
803 result. To mitigate these issues, the surface should be blocked prior to sensing with buffer containing
804 an agent (such as bovine serum albumin) to reach an equilibrium on the surface of the sensor and
805 prevent non-specific interactions from exogenous proteins[153]. Additives to the buffer such as the
806 detergent Tween can further aid in preparing the surface[240]. Furthermore, the sensor itself can be
807 functionalized with antifouling elements such as polymeric scaffolds[241] It has been reported that

surface modification with zwitterionic polymer conjugates can reduce the bulk shift caused by complex biologic matrices, such as serum or plasma, allowing for label-free assays in human samples[242]. However, it is unclear if even the best surface modification can minimize non-specific binding to the point that its contribution to the signal can be ignored relative to the targeted biomolecule[243].

[H1] Outlook

Further advancements in the detection capability of WGM sensors remain possible by using the assembly of plasmonic nanoparticle dimers whose near-field enhancement is much higher than that of monomers[244], improving the Q factor of WGM microcavities in water, and lowering the thermorefractive noise floor **[G]**. Further enhancing sensitivity enables the detection of previously inaccessible molecular properties such as single-molecule chirality[245], new spectroscopy via exciting vibrational modes in proteins[246] and real-time monitoring of light-induced chemical reactions (such as the growth of gold nanorods[247]). For *in vivo* sensing, it would be beneficial to use cavities with even smaller sizes, such as metal-coated disc cavities[248] and spasers[207,249], to perturb the cells less. While finding many important applications in chemistry and biology, the field of WGM sensing is potentially connected to many important and fundamental topics in physics, for example non-Hermitian physics[29], optomechanics[250], the quantum nature of cavity QED[31] and precision measurements with WGM microcombs[30]. Combining WGM micro-interferometers with the measurement techniques developed in quantum optics may stimulate more exciting applications, such as probing single molecules with single photons and analysing single photons emitted from biomolecules[251].

Figures

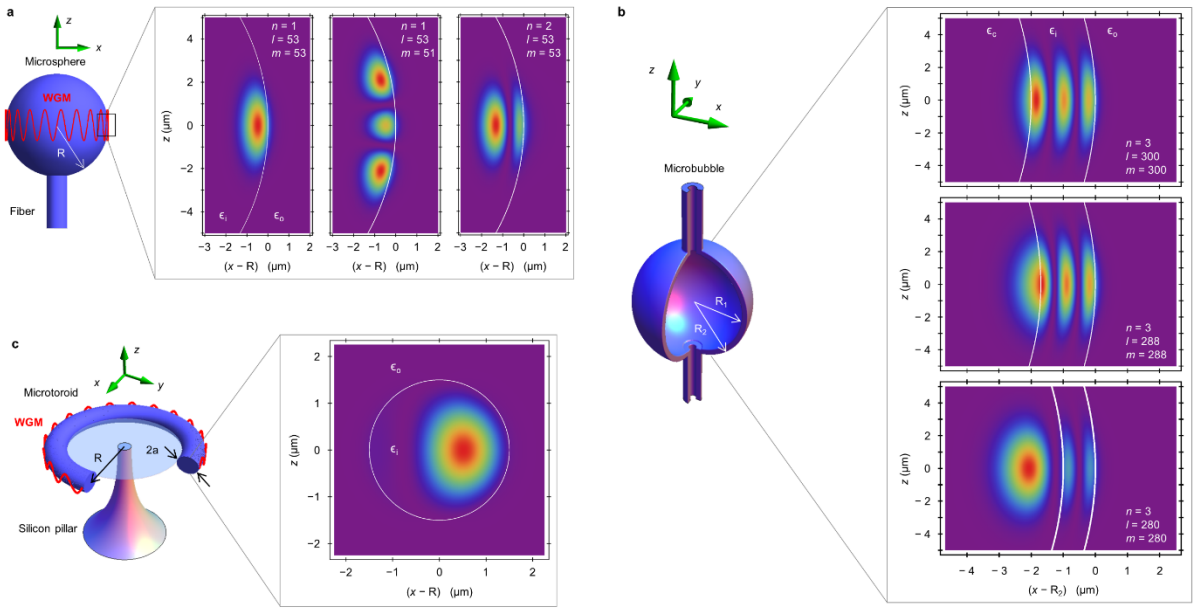

Figure 1. Whispering gallery modes (WGMs) in microspheres, microbubbles and microtoroids. a| A silica (relative permittivity $\epsilon_{\mathrm{i}} = 2.09$) microsphere is fabricated by simply melting the tip of an optical fibre (refractive index of 1.45). The microsphere has a radius $R = 10$ μm and is situated in air (relative permittivity $\epsilon_{\mathrm{o}} = 1$). WGMs circulate at the microsphere's surface. Light intensity distributions of three TE-polarized WGMs around the telecommunication wavelength of 1550 nm are presented. A specific WGM is characterized by radial n, polar l and azimuthal m numbers. **b**| A microbubble (hollow sphere) has an inner radius R_1 and an outer radius $R_2 = 36$ μm. The microbubble is filled with water (i.e., water core) whose relative permittivity is $\epsilon_{\mathrm{c}} = 1.77$. Light intensity distributions of three TE-polarized $(n = 3, l, m = l)$ WGMs around the wavelength 963 nm are displayed, where the inner radius R_1 corresponding to $l = 300$, 288 and 280 is 34, 34.3 and 35 μm, respectively. **c**| A microtoroid consists of a silica microring and a silicon pillar. The geometry of microtoroid is characterized by a major radius $R = 20$ μm and a minor radius $a = 1.5$ μm. Light intensity distribution of the fundamental TE-polarized WGM at 1550 nm is depicted.

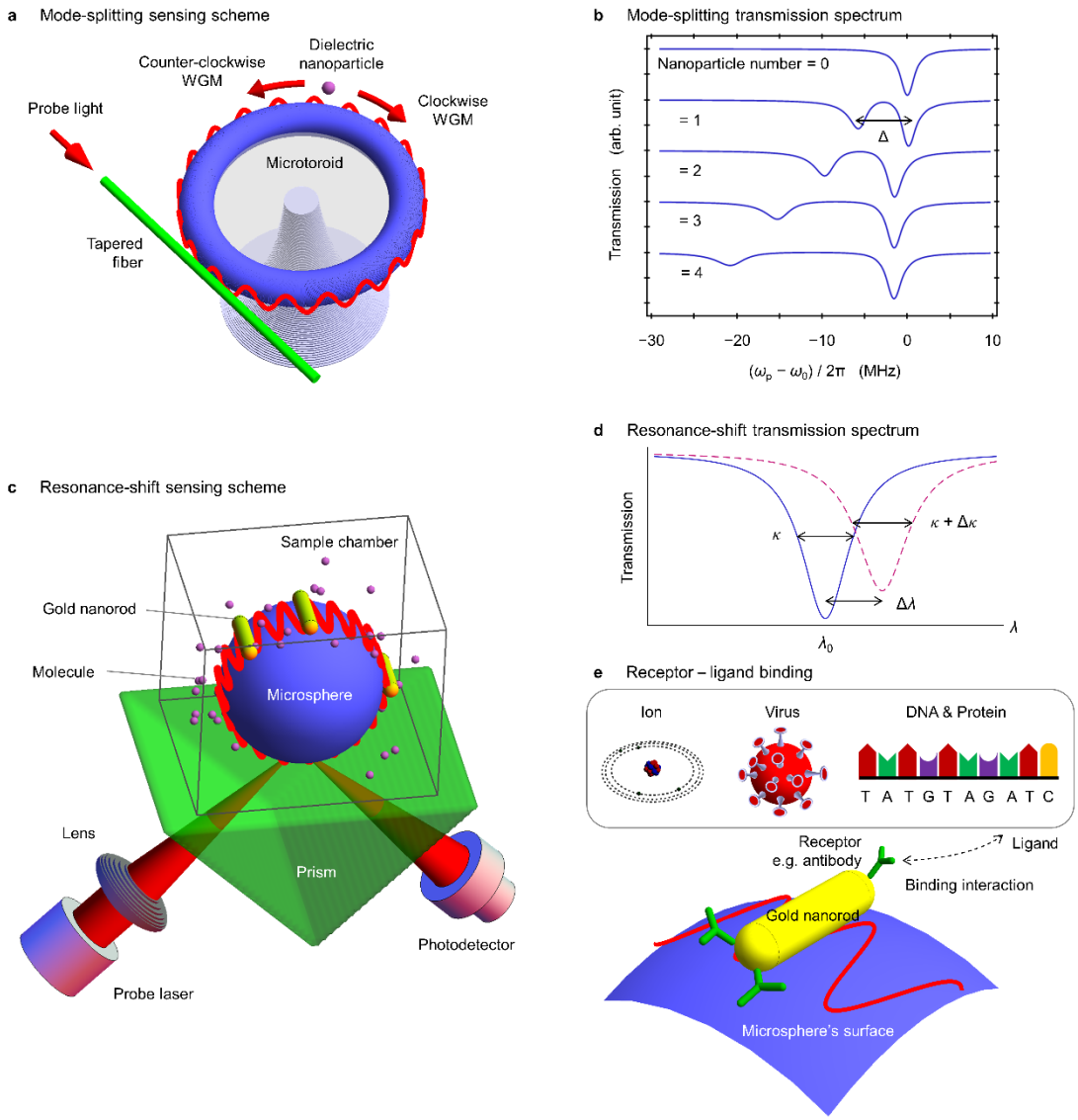

Figure 2. Single-nanoparticle/molecule sensing. a| Mode-splitting sensing scheme. A dielectric nanoparticle (also called a scatterer) is located in the near-field zone of a microtoroid. The scatterer-induced backscattering leads to indirect coupling between two degenerate clockwise and counter-clockwise whispering gallery modes (WGMs). A probe light travels in a tapered fibre that is evanescently coupled with the microtoroid. Single-nanoparticle events can be extracted by measuring the transmission spectrum of the microcavity in real time. **b**| Dependence of numerically simulated transmission spectrum of the microcavity on the number of deposited spherical nanoparticles (radius of 150 nm and relative permittivity of 2.52), where ω_p is the probe beam frequency and Δ denotes the mode splitting. The sensor operates in air. The fundamental TE-polarized WGM at wavelength $\lambda_0 = 1550$ nm (frequency $\omega_0 = 2\pi c/\lambda_0$ and effective mode volume of 5.0×10^{-13} m^3) is applied for sensing. **c**| Schematic diagram of an optoplasmonic sensor. A microsphere is evanescently pumped by a probe laser via an optical prism. The microsphere is immersed in a sample chamber that contains analyte molecules dissolved in solution. Several gold

nanorods are permanently adsorbed onto the microsphere's surface. The localized surface plasmon resonance of gold nanorods boosts the molecule-microcavity interaction. **d**| Sensing scheme based on the resonance wavelength shift. The transmission spectrum (solid) of a bare microcavity shows a spectral linewidth κ around the mode resonance wavelength λ_0. A dielectric nanoparticle/molecule binding to the microcavity's surface shifts the transmission spectrum (dashed) by an amount $\Delta\lambda$ and induces an extra broadening $\Delta\kappa$. **e**| Binding interaction between receptor and ligand molecules. The surface of gold nanorods is modified by receptor sites such as antibodies. The ligand molecules can be ions, viruses, DNA strands or proteins.

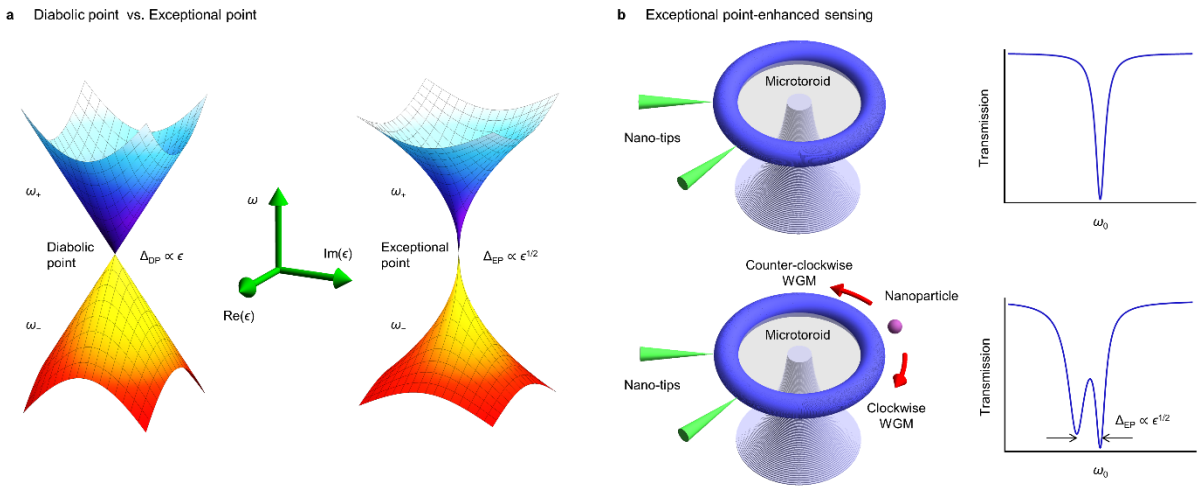

871 **FIGURE 3**. **Exceptional point enhanced sensing. a**| Comparison of the perturbation-induced
872 responses of a system around a two-fold diabolic point and a two-fold exceptional point. The system
873 is composed of two degenerate eigenmodes. When the system is under a perturbation, two modes
874 are weakly coupled with a complex strength ϵ, leading to a splitting between two eigenfrequencies
875 $\omega_{\pm}$. The frequency splitting Δ_{DP} around the diabolic point is proportional to ϵ, whereas the splitting
876 Δ_{EP} around the exceptional point is proportional to $\sqrt{\epsilon}$. **b**| Schematic diagram of whispering gallery
877 mode (WGM)-microcavity-based sensing at a two-fold exceptional point. Two Rayleigh scatterers
878 (here, silica nano-tips) are introduced to ensure the microcavity operates at the exceptional point.
879 The transmission spectrum of the microcavity shows a dip at the mode resonance frequency ω_0. A
880 dielectric nanoparticle is introduced to perturb the microcavity with a strength ϵ. This extra
881 nanoparticle induces an indirect coupling between two degenerate clockwise and counter-clockwise
882 WGMs, resulting in mode splitting Δ_{EP} around ω_0.
883

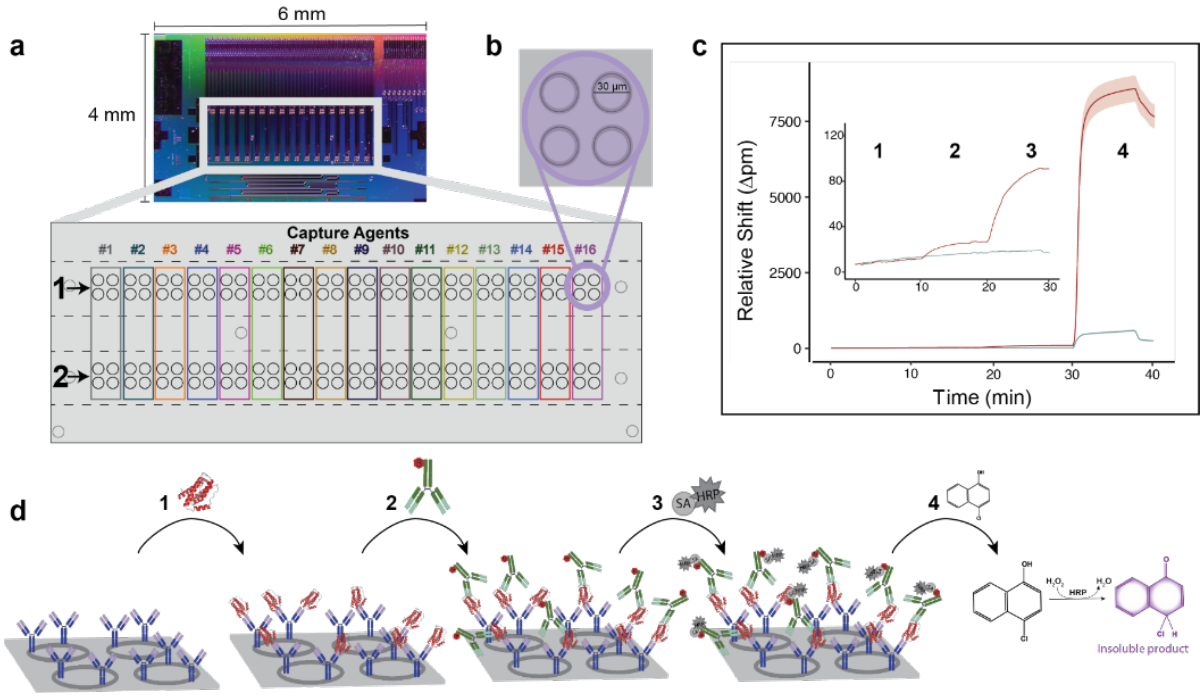

885 **FIGURE 4. Biological sensing using microring resonators. a**| Diagram of a silicon chip
886 integrated with 128 individual sensors. The gray inset highlights the multiplexing capabilities of
887 this sensor geometry, with 16 different capture agents spotted on the clusters of 4 microrings in
888 each of the two microfluidic channels. **b**| The group of four microrings is covered by capture
889 agent solution (blue circle) using microspotting techniques. **c** and **d**| Real-time output of
890 sandwich-style immunoassay (part **d**) on microring resonator. Green trace represents target
891 specific ring response, while blue trace represents response by control spotted rings over the
892 course of the immunoassay steps. The shaded bars represent technical replicates between 4
893 rings. After functionalization of antibodies onto the rings, the sample is flowed across the chip
894 surface and antigen binds to the capture agent, followed by a buffer rinse step (**1**). A biotinylated
895 tracer antibody (**2**), followed by streptavidin-horse radish peroxidase (**3**) are administered, with
896 buffer rinses in between each step. Finally, 4-chloro-1-napthol (**4**) is added as the enzymatic
897 enhancer. When reacted with HRP, this compound results in an insoluble product that drastically
898 alters the refractive index at the sensor surface, leading to lower limits of detection and clinically
899 relevant dynamic ranges.
900

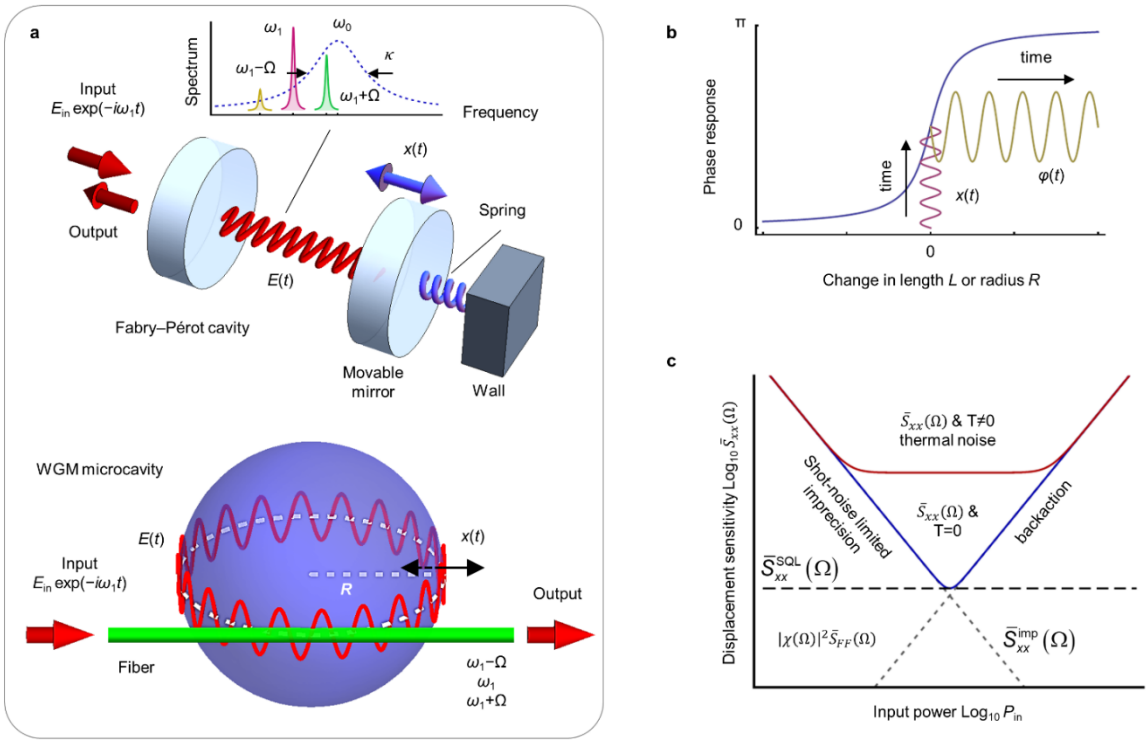

FIGURE 5. Whispering-gallery-mode microcavity-based optomechanics. a| Schematic of optomechanical Fabry–Pérot and whispering-gallery-mode (WGM) systems. The linear Fabry–Pérot cavity contains a movable mirror that is linked to a wall via a spring. The one-dimensional variable $x(t)$ denotes the spring's displacement from its equilibrium position. The WGM microcavity is evanescently coupled with an optical fibre. The displacement $x(t)$ changes the microcavity's radius R, thereby shifting the WGM resonant frequency. In both systems, an input light $E_{\mathrm{in}}e^{-i\omega_1 t}$ at frequency ω_1 pumps the intracavity light field $E(t)$. The resonance frequency and linewidth of the cavity mode are ω_0 and κ, respectively. The radiation pressure causes parametric coupling between optical and mechanical degrees of freedom. When the displacement $x(t)$ follows a sinusoidal oscillation at a radio frequency Ω, the intracavity field $E(t)$ contains three frequency components, i.e., central ω_1, Stokes $\omega_1+\Omega$ and anti-Stokes $\omega_1-\Omega$. **b**| Principal of ultrahigh-sensitivity optomechanical transduction, where the displacement $x(t)$ is mapped onto the phase $\varphi(t)$ of the output field from the microcavity through the phase response curve. **c**| Dependence of the displacement sensitivity $\bar{S}_{xx}(\Omega)$ on the input power $P_{\mathrm{in}} \equiv |E_{\mathrm{in}}|^2$ at temperature T. For a small P_{in}, the shot noise limit $\bar{S}_{xx}^{\mathrm{imp}}(\Omega)$ dominates the sensitivity. By contrast, the quantum backaction noise force primarily influences the mechanical oscillation and the sensitivity is limited to $|\chi(\Omega)|^2\bar{S}_{FF}(\Omega)$ with $\bar{S}_{FF}(\Omega)$ being the spectral density of the backaction noise force and $\chi(\Omega)$ the mechanical susceptibility. At the optimum input power, the displacement sensitivity at $T=0$ is restricted by the standard quantum limit $\bar{S}_{xx}^{\mathrm{SQL}}(\Omega)$. When $T\neq 0$, thermal noise plays a notable role.

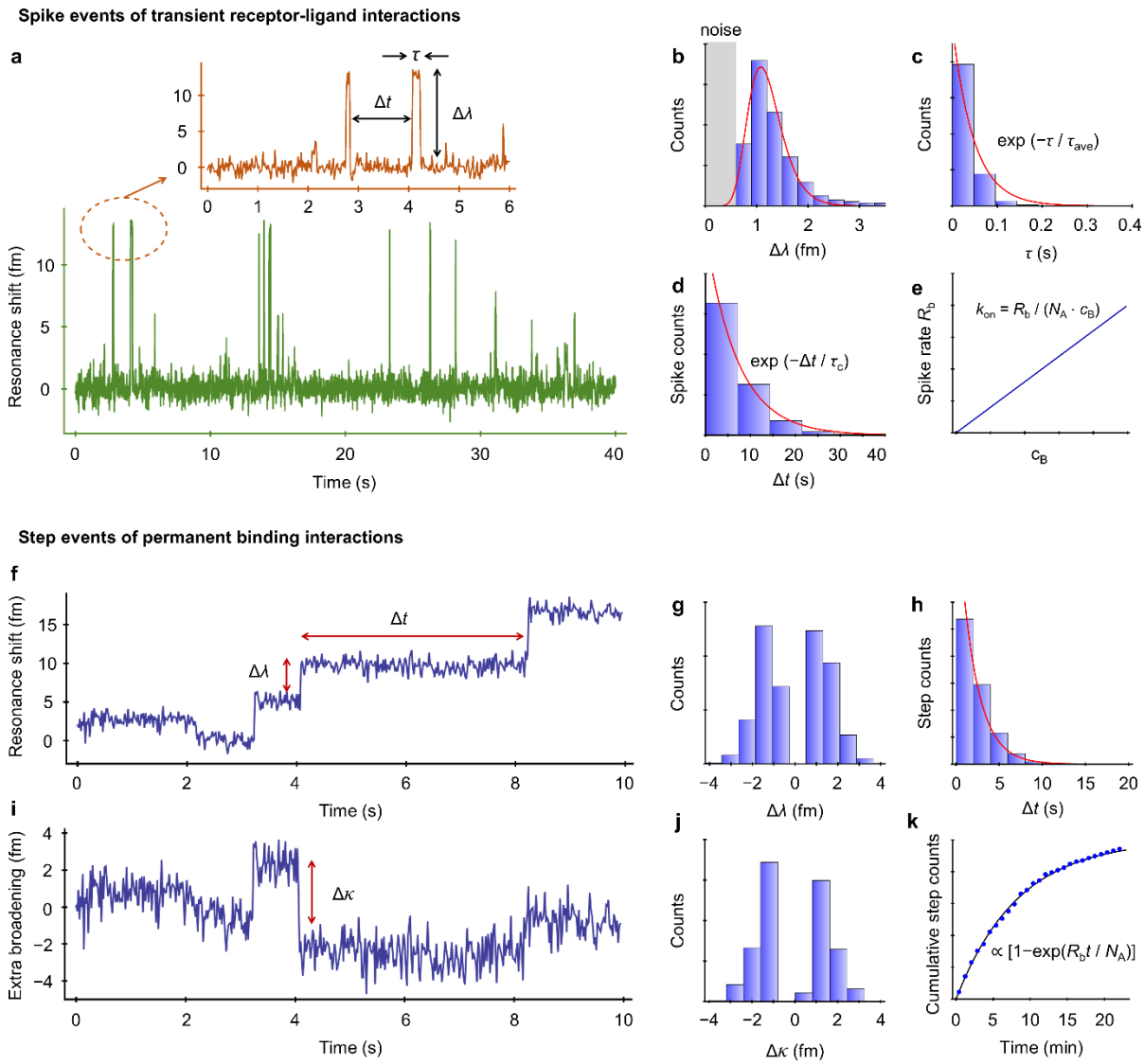

FIGURE 6. Single-molecule detection of optoplasmonic sensors. a–e| Spike events induced by transient receptor-ligand interactions. Spectral spikes in a trace of the WGM resonance wavelength shift represent transient binding events (part **a**). The histogram of spike heights $\Delta\lambda$ presents a lognormal distribution (line), where small $\Delta\lambda$ cannot be identified due to the background noise floor (grey shadow in part **b**). Spike durations τ exhibit an exponential distrubtion $e^{-\tau/\tau_{\mathrm{ave}}}$ (line) with an average value τ_{ave} (part **c**). The interval Δt between two adjecent spikes also follows an exponential distrubtion $e^{-\tau/\tau_{\mathrm{c}}}$ (line) with a decay constant τ_{c}. The total spike rate R_{b} depends linearly on the concentration c_{B} of analyte molecules (part **e**). The kinetic on-rate constant is given by $k_{\mathrm{on}} = R_{\mathrm{b}}/N_{\mathrm{A}}c_{\mathrm{B}}$ with the number N_{A} of receptor sites. **f–k|** Step events in single-molecule detection. When a ligand molecule is permanently bound to a receptor, a step change occurs in the trace of WGM resonance wavelength (part **f**). The histogram of step heights $\Delta\lambda$ shows that $\Delta\lambda$ can be either positive or negative (part **g**). The interval Δt between two adjecent step events follows an exponential distribution (line). Besides monitoring the WGM resonance wavelength, single-molecule

936 detection can be also performed by tracking the extra broadening $\Delta\kappa$ of the WGM linewidth (part **i**).
937 The histogram of $\Delta\kappa$ shows that $\Delta\kappa$ can be either positive or negative (part **j**). The time-dependent
938 cumulative step counts (symbols) exhibit a saturation behaviour $\left(1 - e^{R_b t / N_A}\right)$ (line) due to the
939 consumption of receptor sites (part **k**).
940

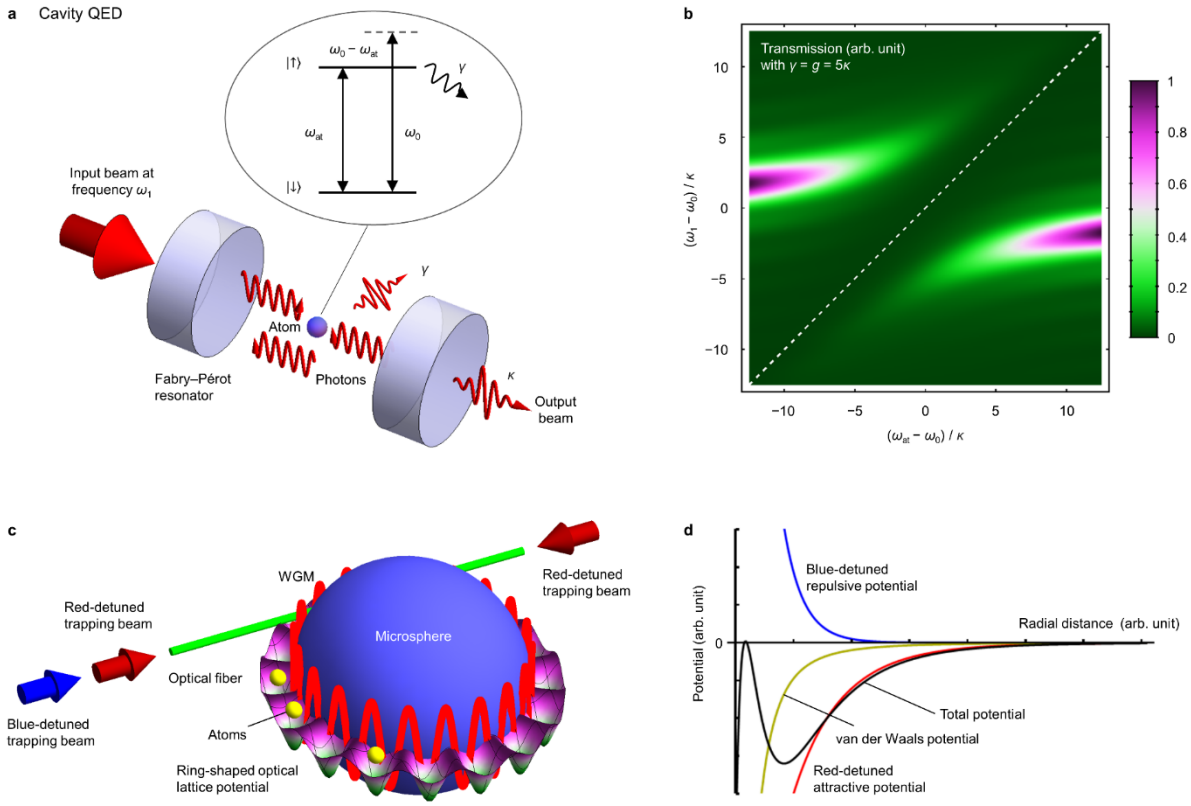

Tables

Table 1 | **Biochemical sensing at single-nanoparticle/molecule level**

Mechanism	Sensor	Environment	Analyte
Mode splitting	Microtoroid	Air	Potassium chloride and polystyrene nanoparticles (radius of 30 nm)[10]
Mode splitting	Toroid-shaped microlaser with heterodyne detection	Air	Polystyrene nanoparticles (radius of 15 nm), gold nanoparticles (radius of 10 nm), and Influenza A virions[92]
Mode splitting	Raman microlaser with heterodyne detection	Water	Polystyrene nanoparticles (radius of 40 nm)[43]
Resonance shift	Microsphere	PBS solution	Polystyrene nanoparticles (radius of 250 nm) and Influenza A virions (radius of 50 nm and mass of 512 ag)[100]
Resonance shift	Microsphere hybridized with gold nanoshell	Water	RNA virus MS2 (radius of 13.6 nm and mass of 6 ag)[102]
Resonance shift	Optoplasmonic sensor	Water	Short singlestranded DNA oligonucleotides[14]
Resonance shift	Optoplasmonic sensor	Water	Zn^{2+} (ionic radius of 0.74 Å) and Hg^{2+} (ionic radius of 1.02 Å)[101]
Resonance shift	Optoplasmonic sensor	Water	Biotinylated poly(ethylene glycol)[104]
Resonance shift	Optoplasmonic sensor	Water	Enzymes[106,185]
Resonance shift	Optoplasmonic sensor	Water	Thiol-disulfide exchange reaction[107]
Resonance shift	Microtoroid with laser-frequency locking	Water	Exosomes (radius of 22 nm and refractive index of 1.375)[197] and interleukin-2 (REF.[198])
Mode broadening	Microtoroid	Air	Lentiviruses[12]
Mode broadening	Microtoroid	Water	Gold nanorods (length of 40 nm and diameter of 16 nm)[111]
Optomechanical spring sensing	Microsphere	Water	BSA proteins with a molecular weight of 66 kDa[183]

An optoplasmonic sensor is composed of a silica microsphere hybridized with gold nanorods. PBS, Phosphate-buffered saline; BSA, Bovine serum albumin; ag, attogram; kDa, kilodalton.

Boxes

[bH1] Box 1 | Fundamentals of WGMs

A specific WGM is characterized by a set of integers (n, l, m) with radial $n \geq 1$, polar $l \geq 0$ and azimuthal $m \in [-l, l]$ numbers. The WGM has n intensity maxima in the radial axis and $(l - |m| + 1)$ intensity maxima along the polar direction (FIG. 1). The positive m represents the optical wave circulating in the clockwise direction while the negative m denotes the counter-

clockwise direction. The fundamental WGMs correspond to $(n = 1, l, m = \pm l)$ with only one intensity maximum in both the radial and polar directions. In addition, a WGM is either transverse magnetic (TM) or transverse electric (TE) polarized. The TM- orTE-polarization denotes light with its magnetic or electric field perpendicular to the plane of incidence, respectively. The resonance frequency of the WGM (n, l, m) with a large l approximates[252] $\omega_{n,l} \approx l\Delta\omega_{\mathrm{FSR}}$, where the free spectral range $\Delta\omega_{\mathrm{FSR}} \equiv c/\sqrt{\epsilon_{\mathrm{i}}}R$ denotes the frequency spacing between two successive WGMs, ϵ_{i} is the relative permittivity of the microcavity's material, and R is the radius of the microcavity. Each frequency $\omega_{n,l}$ has a $(2l + 1)$-fold degeneracy with respect to m. For example, at the telecommunication wavelength $\lambda_0 = 1550$ nm, the fundamental TE-polarized WGM of a silica microsphere ($\epsilon_{\mathrm{i}} = 2.085$ and $R = 50$ μm) in air corresponds to $n = 1, l = 281, m = l$ with $\Delta\omega_{\mathrm{FSR}} = 2\pi \times 0.67$ THz. The finesse $\mathcal{F} = \Delta\omega_{\mathrm{FSR}}/\kappa$ reaches as high as 10^6 for a quality factor Q of 3×10^8 (REF.[8]). Here, $\kappa = \omega_0/Q$ gives the WGM linewidth. When a molecule lands on the microcavity's surface, the circulating light interacts with the molecule $\mathcal{F}$ times, giving rise to a detectable sensing signal.

[bH1] Box 2 | Optical fibre coupler

Despite the total internal reflection at the inner surface of a WGM microcavity, a small amount of intracavity field can penetrate into the surrounding medium and falls off exponentially with distance from the microcavity-surrounding interface. This evanescent channel allows the light to be coupled into and out of the microcavity through, for example, an optical fibre coupler (see Supplementary Fig. 2). That is, the coupler plays both an input and (signal) output role. The power transmission of the light passing the coupling region depends on the fibre-microcavity coupling strength and may be tuned through varying the fibre-microcavity distance (see Supplementary Note 4). For a large distance, the coupling strength is almost zero and the transmission approximates unity. As the fibre is brought into close proximity to the microcavity, the fibre-microcavity coupling strength is enhanced and the transmission decreases in the under-coupling regime. The transmission is minimized at the critical coupling point, where the internal microcavity loss is equal to the fibre-microcavity coupling loss[253] (see Supplementary Fig. 2). As the fibre-microcavity distance is further reduced, the transmission gradually increases in the over-coupling regime.

References

1 Gorodetsky, M. L., Savchenkov, A. A. & Ilchenko, V. S. Ultimate *Q* of optical microsphere resonators. *Opt. Lett.* **21**, 453–455 (1996).

2 Serpengüzel, A., Arnold, S. & Griffel, G. Excitation of resonances of microspheres on an optical fiber. *Opt. Lett.* **20**, 654–656 (1995).

3 Braginsky, V. B., Gorodetsky, M. L. & Ilchenko, V. S. Quality-factor and nonlinear properties of optical whispering-gallery modes. *Phys. Lett. A* **137**, 393–397 (1989).
4 Purcell, E. M. Spontaneous emission probabilities at radio frequencies. *Phys. Rev.* **69**, 681 (1946).
5 Kippenberg, T. J., Spillane, S. M. & Vahala, K. J. Demonstration of ultra-high-Q small mode volume toroid microcavities on a chip. *Appl. Phys. Lett.* **85**, 6113–6115 (2004).
6 Metzger, B. et al. Purcell-enhanced spontaneous emission of molecular vibrations. *Phys. Rev. Lett.* **123**, 153001 (2019).
7 Zhang, J. L. et al. Strongly cavity-enhanced spontaneous emission from silicon-vacancy centers in diamond. *Nano Lett.* **18**, 1360–1365 (2018).
8 Vernooy, D. W., Ilchenko, V. S., Mabuchi, H., Streed, E. W. & Kimble, H. J. High-*Q* measurements of fused-silica microspheres in the near infrared. *Opt. Lett.* **23**, 247–249 (1998).
9 Jiang, X., Qavi, A. J., Huang, S. H. & Yang, L. Whispering-gallery sensors. *Matter* **3**, 371–392 (2020).
10 Zhu, J. et al. On-chip single nanoparticle detection and sizing by mode splitting in an ultrahigh-*Q* microresonator. *Nat. Photon.* **4**, 46–49 (2010).
11 Vollmer, F. et al. Protein detection by optical shift of a resonant microcavity. *Appl. Phys. Lett.* **80**, 4057–4059 (2002).
12 Shao, L. et al. Detection of single nanoparticles and lentiviruses using microcavity resonance broadening. *Adv. Mater.* **25**, 5616–5620 (2013).
13 Chen, Y., Yin, Y., Ma, L. & Schmidt, O. G. Recent progress on optoplasmonic whispering-gallery-mode microcavities. *Adv. Optical Mater.* **9**, 2100143 (2021).
14 Baaske, M. D., Foreman, M. R. & Vollmer, F. Single-molecule nucleic acid interactions monitored on a label-free microcavity biosensor platform. *Nat. Nanotechnol.* **9**, 933–939 (2014).
15 Sumetsky, M. Whispering-gallery-bottle microcavities: the three-dimensional etalon. *Opt. Lett.* **29**, 8–10 (2004).
16 Ward, J. M. et al. Heat-and-pull rig for fiber taper fabrication. *Rev. Sci. Instrum.* **77**, 083105 (2006).
17 Byeon, J.-Y. & Bailey, R. C. Multiplexed evaluation of capture agent binding kinetics using arrays of silicon photonic microring resonators. *Analyst* **136**, 3430–3433 (2011).
18 Scheler, O. et al. Label-free, multiplexed detection of bacterial tmRNA using silicon photonic microring resonators. *Biosens. Bioelectron.* **36**, 56–61 (2012).
19 Qavi, A. J. & Bailey, R. C. Multiplexed detection and label-free quantitation of microRNAs using arrays of silicon photonic microring resonators. *Angew. Chem. Int. Ed.* **49**, 4608–4611 (2010).
20 Humar, M. & Yun, S. H. Intracellular microlasers. *Nat. Photon.* **9**, 572–576 (2015).
21 Schubert, M. et al. Monitoring contractility in cardiac tissue with cellular resolution using biointegrated microlasers. *Nat. Photon.* **14**, 452–458 (2020).
22 Schubert, M. et al. Lasing within live cells containing intracellular optical microresonators for barcode-type cell tagging and tracking. *Nano Lett.* **15**, 5647–5652 (2015).
23 Martino, N. et al. Wavelength-encoded laser particles for massively multiplexed cell tagging. *Nat. Photon.* **13**, 720–727 (2019).
24 Humar, M., Upadhya, A. & Yun, S. H. Spectral reading of optical resonance-encoded cells in microfluidics. *Lab Chip* **17**, 2777–2784 (2017).
25 Densmore, A. et al. Silicon photonic wire biosensor array for multiplexed real-time and label-free molecular detection. *Opt. Lett.* **34**, 3598–3600 (2009).
26 Toropov, N. & Vollmer, F. Whispering-gallery microlasers for cell tagging and barcoding: the prospects for in vivo biosensing. *Light Sci. Appl.* **10**, 77 (2021).

27 He, L., Özdemir, Ş. K. & Yang, L. Whispering gallery microcavity lasers. *Laser Photonics Rev.* **7**, 60–82 (2013).

28 Aspelmeyer, M., Kippenberg, T. J. & Marquardt, F. Cavity optomechanics. *Rev. Mod. Phys.* **86**, 1391–1452 (2014).

29 Özdemir, Ş. K., Rotter, S., Nori, F. & Yang, L. Parity–time symmetry and exceptional points in photonics. *Nat. Mater.* **18**, 783–798 (2019).

30 Diddams, S. A., Vahala, K. & Udem, T. Optical frequency combs: coherently uniting the electromagnetic spectrum. *Science* **369**, eaay3676 (2020).

31 Aoki, T. et al. Observation of strong coupling between one atom and a monolithic microresonator. *Nature* **443**, 671–674 (2006).

32 Sandoghdar, V. et al. Very low threshold whispering-gallery-mode microsphere laser. *Phys. Rev. A* **54**, R1777–R1780 (1996).

33 Zhou, Z., Yin, B. & Michel, J. On-chip light sources for silicon photonics. *Light Sci. Appl.* **4**, e358 (2015).

34 Schliesser, A., Riviere, R., Anetsberger, G., Arcizet, O. & Kippenberg, T. Resolved-sideband cooling of a micromechanical oscillator. *Nat. Phys.* **4**, 415–419 (2008).

35 Schliesser, A., Anetsberger, G., Rivière, R., Arcizet, O. & Kippenberg, T. J. High-sensitivity monitoring of micromechanical vibration using optical whispering gallery mode resonators. *New J. Phys.* **10**, 095015 (2008).

36 Rüter, C. E. et al. Observation of parity-time symmetry in optics. *Nat. Phys.* **6**, 192–195 (2010).

37 Peng, B. et al. Parity–time-symmetric whispering-gallery microcavities. *Nat. Phys.* **10**, 394–398 (2014).

38 Wang, C., Sweeney, W. R., Stone, A. D. & Yang, L. Coherent perfect absorption at an exceptional point. *Science* **373**, 1261–1265 (2021).

39 Newman, Z. L. et al. Architecture for the photonic integration of an optical atomic clock. *Optica* **6**, 680–685 (2019).

40 Buck, J. R. & Kimble, H. J. Optimal sizes of dielectric microspheres for cavity QED with strong coupling. *Phys. Rev. A* **67**, 033806 (2003).

41 Yu, D. & Vollmer, F. Microscale whispering-gallery-mode light sources with lattice-confined atoms. *Sci. Rep.* **11**, 13899 (2021).

42 Vollmer, F. & Yu, D. *Optical Whispering Gallery Modes for Biosensing: From Physical Principles to Applications*. (Springer, Cham, 2020).

43 Li, B.-B. et al. Single nanoparticle detection using split-mode microcavity Raman lasers. *Proc. Natl. Acad. Sci. USA* **111**, 14657–14662 (2014).

44 Özdemir, Ş. K. et al. Highly sensitive detection of nanoparticles with a self-referenced and self-heterodyned whispering-gallery Raman microlaser. *Proc. Natl. Acad. Sci. USA* **111**, E3836–E3844 (2014).

45 Sumetsky, M., Dulashko, Y. & Windeler, R. S. Optical microbubble resonator. *Opt. Lett.* **35**, 898–900 (2010).

46 Li, H. & Fan, X. Characterization of sensing capability of optofluidic ring resonator biosensors. *Appl. Phys. Lett.* **97**, 011105 (2010).

47 Murugan, G. S., Petrovich, M. N., Jung, Y., Wilkinson, J. S. & Zervas, M. N. Hollow-bottle optical microresonators. *Opt. Express* **19**, 20773–20784 (2011).

48 Armani, D. K., Kippenberg, T. J., Spillane, S. M. & Vahala, K. J. Ultra-high-*Q* toroid microcavity on a chip. *Nature* **421**, 925–928 (2003).

49 Oraevsky, A. N. Whispering-gallery waves. *Quantum Electronics* **32**, 377–400 (2002).

50 Barucci, A., Berneschi, S. & Giannetti, A. Optical microbubble resonators with high refractive index inner coating for bio-sensing applications: an analytical approach. *Sensors* **16**, 1992 (2016).

51 Little, B. E., Laine, J.-P. & Haus, H. A. Analytic theory of coupling from tapered fibers and half-blocks into microsphere resonators. *J. Lightwave Technol.* **17**, 704–715 (1999).
52 Louyer, Y., Meschede, D. & Rauschenbeutel, A. Tunable whispering-gallery-mode resonators for cavity quantum electrodynamics. *Phys. Rev. A* **72**, 031801 (2005).
53 Borselli, M. G. *High-Q microresonators as lasing elements for silicon photonics* Dissertation (Ph.D.) thesis, California Institute of Technology, (2006).
54 Michael, C. P. *Optical material characterization using microdisk cavities* Dissertation (Ph.D.) thesis, California Institute of Technology, (2009).
55 Min, B., Yang, L. & Vahala, K. Perturbative analytic theory of an ultrahigh-*Q* toroidal microcavity. *Phys. Rev. A* **76**, 013823 (2007).
56 Balac, S. WGMode: A Matlab toolbox for whispering gallery modes volume computation in spherical optical micro-resonators. *Comput. Phys. Commun.* **243**, 121–134 (2019).
57 Collot, L., Lefèvre-Seguin, V., Brune, M., Raimond, J. M. & Haroche, S. Very high-*Q* whispering-gallery mode resonances observed on fused silica microspheres. *Europhys. Lett.* **23**, 327–334 (1993).
58 Kim, W., Özdemir, Ş. K., Zhu, J. & Yang, L. Observation and characterization of mode splitting in microsphere resonators in aquatic environment. *Appl. Phys. Lett.* **98**, 141106 (2011).
59 Ward, J. M. et al. Nanoparticle sensing beyond evanescent field interaction with a quasi-droplet microcavity. *Optica* **5**, 674–677 (2018).
60 Berneschi, S. et al. High *Q* silica microbubble resonators fabricated by arc discharge. *Opt. Lett.* **36**, 3521–3523 (2011).
61 Lee, W. et al. A quasi-droplet optofluidic ring resonator laser using a micro-bubble. *Appl. Phys. Lett.* **99**, 091102 (2011).
62 Yang, Y., Ward, J. & Nic Chormaic, S. Quasi-droplet microbubbles for high resolution sensing applications. *Opt. Express* **22**, 6881–6898 (2014).
63 Kippenberg, T. J., Spillane, S. M., Min, B. & Vahala, K. J. Theoretical and experimental study of stimulated and cascaded Raman scattering in ultrahigh-*Q* optical microcavities. *IEEE J. Sel. Top. Quantum Electron.* **10**, 1219–1228 (2004).
64 Qian, S.-X., Snow, J. B., Tzeng, H.-M. & Chang, R. K. Lasing droplets: highlighting the liquid-air interface by laser emission. *Science* **231**, 486–488 (1986).
65 Tzeng, H.-M., Wall, K. F., Long, M. B. & Chang, R. K. Laser emission from individual droplets at wavelengths corresponding to morphology-dependent resonances. *Opt. Lett.* **9**, 499–501 (1984).
66 Watkins, A., Ward, J., Wu, Y. & Nic Chormaic, S. Single-input spherical microbubble resonator. *Opt. Lett.* **36**, 2113–2115 (2011).
67 Borselli, M., Johnson, T. J. & Painter, O. Beyond the Rayleigh scattering limit in high-*Q* silicon microdisks: theory and experiment. *Opt. Express* **13**, 1515–1530 (2005).
68 Chen, C. et al. Effects of edge inclination angles on whispering-gallery modes in printable wedge microdisk lasers. *Opt. Express* **26**, 233–241 (2018).
69 Zhang, X., Liu, L. & Xu, L. Ultralow sensing limit in optofluidic micro-bottle resonator biosensor by self-referenced differential-mode detection scheme. *Appl. Phys. Lett.* **104**, 033703 (2014).
70 Stoian, R.-I., Bui, K. V. & Rosenberger, A. T. Silica hollow bottle resonators for use as whispering gallery mode based chemical sensors. *J. Opt.* **17**, 125011 (2015).
71 Yang, D. et al. Real-time monitoring of hydrogel phase transition in an ultrahigh *Q* microbubble resonator. *Photon. Res.* **8**, 497–502 (2020).
72 Guo, Y., Zhang, Y., Su, H., Zhu, F., Yi, G. & Wang, J. Magnetic-field tuning whispering gallery mode based on hollow microbubble resonator with Terfenol-D-fixed. *Appl. Opt.* **58**, 8889–8893 (2019).
73 Henze, R., Seifert, T., Ward, J. & Benson, O. Tuning whispering gallery modes using internal aerostatic pressure. *Opt. Lett.* **36**, 4536–4538 (2011).

74 Hall, J. M. M. et al. Determining the geometric parameters of microbubble resonators from their spectra. *J. Opt. Soc. Am. B* **34**, 44–51 (2017).
75 Cosci, A. et al. Confocal reflectance microscopy for determination of microbubble resonator thickness. *Opt. Express* **23**, 16693–16701 (2015).
76 Lei, F., Ward, J. M., Romagnoli, P. & Nic Chormaic, S. Polarization-controlled cavity input-output relations. *Phys. Rev. Lett.* **124**, 103902 (2020).
77 Grossmann, T. et al. Direct laser writing for active and passive high-*Q* polymer microdisks on silicon. *Opt. Express* **19**, 11451–11456 (2011).
78 Lin, J. et al. On-chip three-dimensional high-Q microcavities fabricated by femtosecond laser direct writing. *Opt. Express* **20**, 10212–10217 (2012).
79 Toropov, N., Zaki, S., Vartanyan, T. & Sumetsky, M. Microresonator devices lithographically introduced at the optical fiber surface. *Opt. Lett.* **46**, 1784–1787 (2021).
80 Knapper, K. A., Heylman, K. D., Horak, E. H. & Goldsmith, R. H. Chip-scale fabrication of high-*Q* all-glass toroidal microresonators for single-particle label-free imaging. *Adv. Mater.* **28**, 2945–2950 (2016).
81 Kippenberg, T. J., Spillane, S. M. & Vahala, K. J. Modal coupling in traveling-wave resonators. *Opt. Lett.* **27**, 1669–1671 (2002).
82 Knight, J. C., Cheung, G., Jacques, F. & Birks, T. A. Phase-matched excitation of whispering-gallery-mode resonances by a fiber taper. *Opt. Lett.* **22**, 1129–1131 (1997).
83 Gorodetsky, M. L. & Ilchenko, V. S. Optical microsphere resonators: optimal coupling to high-*Q* whispering-gallery modes. *J. Opt. Soc. Am. B* **16**, 147–154 (1999).
84 Vassiliev, V. V. et al. Narrow-line-width diode laser with a high-Q microsphere resonator. *Opt. Commun.* **158**, 305–312 (1998).
85 Hosseini, E. S., Yegnanarayanan, S., Atabaki, A. H., Soltani, M. & Adibi, A. High quality planar silicon nitride microdisk resonators for integrated photonics in the visible wavelength range. *Opt. Express* **17**, 14543–14551 (2009).
86 Zhu, J. et al. Interfacing whispering-gallery microresonators and free space light with cavity enhanced Rayleigh scattering. *Sci. Rep.* **4**, 6396 (2014).
87 Spillane, S. M., Kippenberg, T. J., Painter, O. J. & Vahala, K. J. Ideality in a fiber-taper-coupled microresonator system for application to cavity quantum electrodynamics. *Phys. Rev. Lett.* **91**, 043902 (2003).
88 Arnold, S., Khoshsima, M., Teraoka, I., Holler, S. & Vollmer, F. Shift of whispering-gallery modes in microspheres by protein adsorption. *Opt. Lett.* **28**, 272–274 (2003).
89 Sumetsky, M. Slow light optofluidics: a proposal. *Opt. Lett.* **39**, 5578–5581 (2014).
90 Weiss, D. S. et al. Splitting of high-*Q* Mie modes induced by light backscattering in silica microspheres. *Opt. Lett.* **20**, 1835–1837 (1995).
91 He, L., Ozdemir, S. K., Zhu, J. & Yang, L. Scatterer induced mode splitting in poly(dimethylsiloxane) coated microresonators. *Appl. Phys. Lett.* **96**, 221101 (2010).
92 He, L., Özdemir, Ş. K., Zhu, J., Kim, W. & Yang, L. Detecting single viruses and nanoparticles using whispering gallery microlasers. *Nat. Nanotechnol.* **6**, 428–432 (2011).
93 Kim, W., Özdemir, Ş. K., Zhu, J., He, L. & Yang, L. Demonstration of mode splitting in an optical microcavity in aqueous environment. *Appl. Phys. Lett.* **97**, 071111 (2010).
94 Toropov, N. A. S., M. Permanent matching of coupled optical bottle resonators with better than 0.16 GHz precision. *Opt. Lett.* **41**, 2278–2281 (2016).
95 Vitullo, D. L. P. et al. Tunable SNAP microresonators via internal ohmic heating. *Opt. Lett.* **43**, 4316–4319 (2018).
96 Vollmer, F. & Arnold, S. Whispering-gallery-mode biosensing: label-free detection down to single molecules. *Nat. Methods* **5**, 591–596 (2008).
97 Arnold, S. et al. Whispering gallery mode carousel – a photonic mechanism for enhanced nanoparticle detection in biosensing. *Opt. Express* **17**, 6230–6238 (2009).

98 Gardosi, G., Mangan, B. J., Puc, G. S. & Sumetsky, M. Photonic microresonators created by slow optical cooking. *ACS Photonics* **8**, 436–442 (2021).
99 Yu, D. & Vollmer, F. Allan deviation tells the binding properties in single-molecule sensing with whispering-gallery-mode optical microcavities. *Phys. Rev. Research* **3**, 023087 (2021).
100 Vollmer, F., Arnold, S. & Keng, D. Single virus detection from the reactive shift of a whispering-gallery mode. *Proc. Natl. Acad. Sci. USA* **105**, 20701–20704 (2008).
101 Baaske, M. D. & Vollmer, F. Optical observation of single atomic ions interacting with plasmonic nanorods in aqueous solution. *Nat. Photon.* **10**, 733–739 (2016).
102 Dantham, V. R., Holler, S., Kolchenko, V., Wan, Z. & Arnold, S. Taking whispering gallery-mode single virus detection and sizing to the limit. *Appl. Phys. Lett.* **101**, 043704 (2012).
103 Dantham, V. R. et al. Label-free detection of single protein using a nanoplasmonic-photonic hybrid microcavity. *Nano Lett.* **13**, 3347–3351 (2013).
104 Kim, E., Baaske, M. D. & Vollmer, F. In situ observation of single-molecule surface reactions from low to high affinities. *Adv. Mater.* **28**, 9941–9948 (2016).
105 Shopova, S. I., Rajmangal, R., Holler, S. & Arnold, S. Plasmonic enhancement of a whispering-gallery-mode biosensor for single nanoparticle detection. *Appl. Phys. Lett.* **98**, 243104 (2011).
106 Subramanian, S. et al. Sensing enzyme activation heat capacity at the single-molecule level using gold-nanorod-based optical whispering gallery modes. *ACS Appl. Nano Mater.* **4**, 4576–4583 (2021).
107 Vincent, S., Subramanian, S. & Vollmer, F. Optoplasmonic characterisation of reversible disulfide interactions at single thiol sites in the attomolar regime. *Nat. Commun.* **11**, 2043 (2020).
108 Swaim, J. D., Knittel, J. & Bowen, W. P. Detection limits in whispering gallery biosensors with plasmonic enhancement. *Appl. Phys. Lett.* **99**, 243109 (2011).
109 Willets, K. A. & Van Duyne, R. P. Localized surface plasmon resonance spectroscopy and sensing. *Annu. Rev. Phys. Chem.* **58**, 267–297 (2007).
110 Eerqing, N. et al. Comparing transient oligonucleotide hybridization kinetics using DNA-PAINT and optoplasmonic single-molecule sensing on gold nanorods. *arXiv:2103.07520* (2021).
111 Shen, B.-Q. et al. Detection of single nanoparticles using the dissipative interaction in a high-*Q* microcavity. *Phys. Rev. Applied* **5**, 024011 (2016).
112 Jiang, X.-F. et al. Highly unidirectional emission and ultralow-threshold lasing from on-chip ultrahigh-*Q* microcavities. *Adv. Mater.* **24**, OP260–OP264 (2012).
113 Shao, L. et al. Ultrahigh-*Q*, largely deformed microcavities coupled by a free-space laser beam. *Appl. Phys. Lett.* **103**, 121102 (2013).
114 Ballard, Z., Baaske, M. D. & Vollmer, F. Stand-off biodetection with free-space coupled asymmetric microsphere cavities. *Sensors* **15**, 8968–8980 (2015).
115 Wiersig, J. Enhancing the sensitivity of frequency and energy splitting detection by using exceptional points: application to microcavity sensors for single-particle detection. *Phys. Rev. Lett.* **112**, 203901 (2014).
116 Wiersig, J. Sensors operating at exceptional points: general theory. *Phys. Rev. A* **93**, 033809 (2016).
117 Miri, M.-A. & Alù, A. Exceptional points in optics and photonics. *Science* **363**, eaar7709 (2019).
118 Chen, W., Özdemir, Ş. K., Zhao, G., Wiersig, J. & Yang, L. Exceptional points enhance sensing in an optical microcavity. *Nature* **548**, 192–196 (2017).
119 Feng, L., Wong, Z. J., Ma, R.-M., Wang, Y. & Zhang, X. Single-mode laser by parity-time symmetry breaking. *Science* **346**, 972–975 (2014).
120 Chen, P.-Y. et al. A. Generalized parity–time symmetry condition for enhanced sensor telemetry. *Nat. Electron.* **1**, 297–304 (2018).

121 Dong, Z., Li, Z., Yang, F., Qiu, C.-W. & Ho, J. S. Sensitive readout of implantable microsensors using a wireless system locked to an exceptional point. *Nat. Electron.* **2**, 335–342 (2019).
122 Park, J.-H. et al. Symmetry-breaking-induced plasmonic exceptional points and nanoscale sensing. *Nat. Phys.* **16**, 462–468 (2020).
123 Hodaei, H. et al. Enhanced sensitivity at higher-order exceptional points. *Nature* **548** 187–191 (2017).
124 Hokmabadi, M. P., Schumer, A., Christodoulides, D. N. & Khajavikhan, M. Non-Hermitian ring laser gyroscopes with enhanced Sagnac sensitivity. *Nature* **576**, 70–74 (2019).
125 Lai, Y.-H., Lu, Y.-K., Suh, M.-G., Yuan, Z. & Vahala, K. Observation of the exceptional-point-enhanced Sagnac effect. *Nature* **576**, 65–69 (2019).
126 Cerjan, A. et al. Experimental realization of a Weyl exceptional ring. *Nat. Photon.* **13**, 623–628 (2019).
127 Zhang, X., Ding, K., Zhou, X., Xu, J. & Jin, D. Experimental observation of an exceptional surface in synthetic dimensions with magnon polaritons. *Phys. Rev. Lett.* **123**, 237202 (2019).
128 Zhen, B. et al. Spawning rings of exceptional points out of Dirac cones. *Nature* **525**, 354–358 (2015).
129 Spillane, S. M., Kippenberg, T. J. & Vahala, K. J. Ultralow-threshold Raman laser using a spherical dielectric microcavity. *Nature* **415**, 621–623 (2002).
130 Humar, M., Dobravec, A., Zhao, X. & Yun, S. H. Biomaterial microlasers implantable in the cornea, skin, and blood. *Optica* **4**, 1080–1085 (2017).
131 Ta, V. D., Caixeiro, S., Fernandes, F. M. & Sapienza, R. Microsphere solid-state biolasers. *Adv. Opt. Mater.* **5**, 1601022 (2017).
132 Van Nguyen, T., Mai, H. H., Van Nguyen, T., Duong, D. C. & Ta, V. D. Egg white based biological microlasers. *J. Phys. D: Appl. Phys.* **53**, 445104 (2020).
133 Wei, Y. et al. Starch-based biological microlasers. *ACS Nano* **11**, 597–602 (2017).
134 Fikouras, A. H. et al. Non-obstructive intracellular nanolasers. *Nat. Commun.* **9**, 4817 (2018).
135 Nizamoglu, S., Gather, M. C. & Yun, S. H. All-biomaterial laser using vitamin and biopolymers. *Adv. Mater.* **25**, 5943–5947 (2013).
136 Chen, Y.-C., Chen, Q. & Fan, X. Optofluidic chlorophyll lasers. *Lab Chip* **16**, 2228–2235 (2016).
137 Jonáš, A. et al. A. *In vitro* and *in vivo* biolasing of fluorescent proteins suspended in liquid microdroplet cavities. *Lab Chip* **14**, 3093–3100 (2014).
138 Fernandez-Bravo, A. et al. Continuous-wave upconverting nanoparticle microlasers. *Nat. Nanotechnol.* **13**, 572–577 (2018).
139 Weller, A., Liu, F. C., Dahint, R. & Himmelhaus, M. Whispering gallery mode biosensors in the low-*Q* limit. *Appl. Phys. B* **90**, 561–567 (2008).
140 Schubert, M. et al. Lasing in live mitotic and non-phagocytic cells by efficient delivery of microresonators. *Sci. Rep.* **7**, 40877 (2017).
141 Reynolds, T. et al. Dynamic self-referencing approach to whispering gallery mode biosensing and its application to measurement within undiluted serum. *Anal. Chem.* **88**, 4036–4040 (2016).
142 Chen, Y.-C., Chen, Q. & Fan, X. Lasing in blood. *Optica* **3**, 809–815 (2016).
143 Vos, K. D., Bartolozzi, I., Schacht, E., Bienstman, P. & Baets, R. Silicon-on-Insulator microring resonator for sensitive and label-free biosensing. *Opt. Express* **15**, 7610–7615 (2007).
144 Iqbal, M. et al. Label-free biosensor arrays based on silicon ring resonators and high-speed optical scanning instrumentation. *IEEE J. Sel. Top. Quant.* **16**, 654–661 (2010).
145 Bailey, R. C. et al. A robust silicon photonic platform for multiparameter biological analysis. *Proc. SPIE* **7220**, 72200N–72201N (2009).
146 Luchansky, M. S. et al. Characterization of the evanescent field profile and bound mass sensitivity of a label-free silicon photonic microring resonator biosensing platform. *Biosens. Bioelectron.* **26**, 1283–1291 (2010).

147 Tsai, D. P., Jackson, H. E., Reddick, R. C., Sharp, S. H. & Warmack, R. J. Photon scanning tunneling microscope study of optical waveguides. *Appl. Phys. Lett.* **56**, 1515–1517 (1990).
148 Hutchinson, A. M. Evanescent wave biosensors. *Mol. Biotechnol.* **3**, 47–54 (1995).
149 Ramachandran, A. et al. A universal biosensing platform based on optical micro-ring resonators. *Biosens. Bioelectron.* **23**, 939–944 (2008).
150 Wu, S., Guo, Y., Wang, W., Zhou, J. & Zhang, Q. Label-free biosensing using a microring resonator integrated with poly-(dimethylsiloxane) microfluidic channels. *Rev. Sci. Instrum.* **90**, 035004 (2019).
151 Washburn, A. L., Gunn, L. C. & Bailey, R. C. Label-free quantitation of a cancer biomarker in complex media using silicon photonic microring resonators. *Anal. Chem.* **81**, 9499–9506 (2009).
152 Shia, W. W. & Bailey, R. C. Single domain antibodies for the detection of ricin using silicon photonic microring resonator arrays. *Anal. Chem.* **85**, 805–810 (2013).
153 Robison, H. M. & Bailey, R. C. A guide to quantitative biomarker assay development using whispering gallery mode biosensors. *Curr. Prot. Chem. Biol.* **9**, 158–173 (2017).
154 Arnfinnsdottir, N. B., Chapman, C. A., Bailey, R. C., Aksnes, A. & Stokke, B. T. Impact of silanization parameters and antibody immobilization strategy on binding capacity of photonic ring resonators. *Sensors* **20**, 3163 (2020).
155 Lange, N., Dietrich, P. M., Lippitz, A., Kulak, N. & Unger, W. E. S. New azidation methods for the functionalization of silicon nitride and application in copper-catalyzed azide-alkyne cycloaddition (CuAAC). *Surf. Interface Anal.* **48**, 621–625 (2016).
156 McClellan, M. S., Domier, L. L. & Bailey, R. C. Label-free virus detection using silicon photonic microring resonators. *Biosens. Bioelectron.* **31**, 388–392 (2012).
157 Medfisch, S. M., Muehl, E. M., Morrissey, J. H. & Bailey, R. C. Phosphatidylethanolamine-phosphatidylserine binding synergy of seven coagulation factors revealed using Nanodisc arrays on silicon photonic sensors. *Sci. Rep.* **10**, 17407 (2020).
158 Kim, K. W. et al. Label-free, PCR-free chip-based detection of telomerase activity in bladder cancer cells. *Biosens. Bioelectron.* **45**, 152–157 (2013).
159 Qavi, A. J., Kindt, J. T., Gleeson, M. A. & Bailey, R. C. Anti-DNA:RNA antibodies and silicon photonic microring resonators: increased sensitivity for multiplexed microRNA detection. *Anal. Chem.* **83**, 5949–5956 (2011).
160 Luchansky, M. S. & Bailey, R. C. Silicon photonic microring resonators for quantitative cytokine detection and T-cell secretion analysis. *Anal. Chem.* **82**, 1975–1981 (2010).
161 Luchansky, M. S., Washburn, A. L., McClellan, M. S. & Bailey, R. C. Sensitive on-chip detection of a protein biomarker in human serum and plasma over an extended dynamic range using silicon photonic microring resonators and sub-micron beads. *Lab Chip* **11**, 2042–2044 (2011).
162 Valera, E., McClellan, M. S. & Bailey, R. C. Magnetically-actuated, bead-enhanced silicon photonic immunosensor. *Anal. Methods* **7**, 8539–8544 (2015).
163 Robison, H. M. et al. Precision immunoprofiling to reveal diagnostic signatures for latent tuberculosis infection and reactivation risk stratification. *Integr. Biol.* **11**, 16–25 (2019).
164 Kindt, J. T., Luchansky, M. S., Qavi, A. J., Lee, S.-H. & Bailey, R. C. Subpicogram per milliliter detection of interleukins using silicon photonic microring Resonators and an enzymatic signal enhancement strategy. *Anal. Chem.* **85**, 10653–10657 (2013).
165 Bidwell, D. E., Buck, A. A. & Diesfend, H. J. The enzyme-linked immunosorbent assay (ELISA). *Bull. World Health Organ.* **54**, 129–139 (1976).
166 Wu, C., Maley, A. M. & Walt, D. R. Single-molecule measurements in microwells for clinical applications. *Crit. Rev. Clin. Lab. Sci.* **57**, 270–290 (2020).
167 Wade, J. H. & Bailey, R. C. Applications of optical microcavity resonators in analytical chemistry. *Annu. Rev. Anal. Chem.* **9**, 1–25 (2016).
168 Kessler, T. et al. A sub-40-mHz-linewidth laser based on a silicon single-crystal optical cavity. *Nat. Photon.* **6**, 687–692 (2012).

169 Matei, D. G. et al. 1.5 µm lasers with sub-10 mHz linewidth. *Phys. Rev. Lett.* **118**, 263202 (2017).
170 Rempe, G., Thompson, R. J., Kimble, H. J. & Lalezari, R. Measurement of ultralow losses in an optical interferometer. *Opt. Lett.* **17**, 363–365 (1992).
171 Rafferty, A., Gorkowski, K., Zuend, A. & Preston, T. C. Optical deformation of single aerosol particles. *Proc. Natl. Acad. Sci. U.S.A* **116**, 19880–19886 (2019).
172 Li, B.-B. et al. Quantum enhanced optomechanical magnetometry. *Optica* **5**, 850–856 (2018).
173 Otterpohl, A. et al. Squeezed vacuum states from a whispering gallery mode resonator. *Optica* **6**, 1375–1380 (2019).
174 Braginsky, V. B. & Khalili, F. Y. *Quantum Measurement*. (Cambridge University Press, 1992).
175 Yuen, H. P. & Chan, V. W. S. Noise in homodyne and heterodyne detection. *Opt. Lett.* **8**, 177–179 (1983).
176 Caniard, T., Briant, T., Cohadon, P.-F., Pinard, M. & Heidmann, A. Ultrasensitive optical measurement of thermal and quantum noises. *Opt. Spectrosc.* **103**, 225–230 (2007).
177 Hadjar, Y., Cohadon, P. F., Aminoff, C. G.,Pinard, M. & Heidmann, A. High-sensitivity optical measurement of mechanical Brownian motion. *Europhys. Lett.* **47**, 545–551 (1999).
178 Lee, K. H., McRae, T. G., Harris, G. I., Knittel, J. & Bowen, W. P. Cooling and control of a cavity optoelectromechanical system. *Phys. Rev. Lett.* **104**, 123604 (2010).
179 Hansch, T. W. & Couillaud, B. Laser frequency stabilization by polarization spectroscopy of a reflecting reference cavity. *Opt. Commun.* **35**, 441–444 (1980).
180 Drever, R. W. P. et al. Laser phase and frequency stabilization using an optical resonator. *Appl. Phys. B* **31**, 97–105 (1983).
181 Li, Y. L., Millen, J. & Barker, P. F. Simultaneous cooling of coupled mechanical oscillators using whispering gallery mode resonances. *Opt. Express* **24**, 1392–1401 (2016).
182 Zullo, R. et al. Laser-frequency locking to a whispering-gallery-mode cavity by spatial interference of scattered light. *Opt. Lett.* **41**, 650–652 (2016).
183 Yu, W., Jiang, W. C., Lin, Q. & Lu, T. Cavity optomechanical spring sensing of single molecules. *Nat. Commun.* **7**, 12311 (2016).
184 Ma, R. et al. Radiation-pressure-driven vibrational modes in ultrahigh-*Q* silica microspheres. *Opt. Lett.* **32**, 2200–2202 (2007).
185 Kim, E., Baaske, M. D., Schuldes, I., Wilsch, P. S. & Vollmer, F. Label-free optical detection of single enzyme-reactant reactions and associated conformational changes. *Sci. Adv.* **3**, e1603044 (2017).
186 Subramanian, S., Vincent, S. & Vollmer, F. Effective linewidth shifts in single-molecule detection using optical whispering gallery modes. *Appl. Phys. Lett.* **117**, 151106 (2020).
187 Förtsch, M. et al. A versatile source of single photons for quantum information processing. *Nat. Commun.* **4**, 1818 (2013).
188 Naweed, A., Farca, G., Shopova, S. I. & Rosenberger, A. T. Induced transparency and absorption in coupled whispering-gallery microresonators. *Phys. Rev. A* **71**, 043804 (2005).
189 Peng, B., Özdemir, Ş. K., Chen, W., Nori, F. & Yang, L. What is and what is not electromagnetically induced transparency in whispering-gallery microcavities. *Nat. Commun.* **5**, 5082 (2014).
190 Totsuka, K., Kobayashi, N. & Tomita, M. Slow light in coupled-resonator-induced transparency. *Phys. Rev. Lett.* **98**, 213904 (2007).
191 Guarino, A., Poberaj, G., Rezzonico, D., Degl'Innocenti, R. & Günter, P. Electro–optically tunable microring resonators in lithium niobate. *Nat. Photon.* **1**, 407–410 (2007).
192 Fürst, J. U. et al. Naturally phase-matched second-harmonic generation in a whispering-gallery-mode resonator. *Phys. Rev. Lett.* **104**, 153901 (2010).
193 Kippenberg, T. J., Spillane, S. M. & Vahala, K. J. Kerr-nonlinearity optical parametric oscillation in an ultrahigh-Q toroid microcavity. *Phys. Rev. Lett.* **93**, 083904 (2004).

194 Savchenkov, A. A. et al. Low threshold optical oscillations in a whispering gallery mode CaF_2 resonator. *Phys. Rev. Lett.* **93**, 243905 (2004).
195 Del'Haye, P. et al. Octave spanning tunable frequency comb from a microresonator. *Phys. Rev. Lett.* **107**, 063901 (2011).
196 Vollmer, F., Arnold, S., Braun, D., Teraoka, I. & Libchaber, A. Multiplexed DNA quantification by spectroscopic shift of two microsphere cavities. *Biophys. J.* **85**, 1974–1979 (2003).
197 Su, J. Label-free single exosome detection using frequency-locked microtoroid optical resonators. *ACS Photonics* **2**, 1241−1245 (2015).
198 Su, J., Goldberg, A. FG & Stoltz, B. M. Label-free detection of single nanoparticles and biological molecules using microtoroid optical resonators. *Light Sci. Appl.* **5**, e16001 (2016).
199 Francois, A. & Himmelhaus, M. Optical sensors based on whispering gallery modes in fluorescent microbeads: size dependence and influence of substrate. *Sensors* **9**, 6836–6852 (2009).
200 Zijlstra, P., van der Molen, K. L. & Mosk, A. P. Spatial refractive index sensor using whispering gallery modes in an optically trapped microsphere. *Appl. Phys. Lett.* **90**, 161101 (2007).
201 Mehrabani, S., Kwong, P., Gupta, M. & Armani, A. M. Hybrid microcavity humidity sensor. *Appl. Phys. Lett.* **102**, 241101 (2013).
202 Wang, Y. et al. Detecting enzymatic reactions in penicillinase via liquid crystal microdroplet-based pH sensor. *Sens. Actuators B Chem.* **258**, 1090–1098 (2018).
203 Yuan, Z. et al. Bioresponsive microlasers with tunable lasing wavelength. *Nanoscale* **13**, 1608–1615 (2021).
204 Manzo, M., Cavazos, O., Ramirez-Cedillo, E. & Siller, H. R. Embedded spherical microlasers for *in vivo* diagnostic biomechanical performances. *J. Eng. Sci. Med. Diagnostics Ther.* **3**, 044504 (2020).
205 Roca-Cusachs, P., Conte, V. & Trepat, X. Quantifying forces in cell biology. *Nat. Cell Biol.* **19**, 742–751 (2017).
206 Cho, S., Humar, M., Martino, N. & Yun, S. H. Laser particle stimulated emission microscopy. *Phys. Rev. Lett.* **117**, 193902 (2016).
207 Gao, Z. et al. Spaser nanoparticles for ultranarrow bandwidth STED super-resolution imaging. *Adv. Mater.* **32**, 1907233 (2020).
208 Macek, W. M. & Davis Jr., D. T. M. Rotation rate sensing with traveling-wave ring lasers. *Appl. Phys. Lett.* **2**, 67–68 (1963).
209 Liang, W. et al. Resonant microphotonic gyroscope. *Optica* **4**, 114–117 (2017).
210 Wang, J., Feng, L., Tang, Y. & Zhi, Y. Resonator integrated optic gyro employing trapezoidal phase modulation technique. *Opt. Lett.* **40**, 155–158 (2015).
211 Ma, H. et al. Resonant micro-optic gyro using a short and high-finesse fiber ring resonator. *Opt. Lett.* **40**, 5862–5865 (2015).
212 Ma, H., Zhang, J., Wang, L. & Jin, Z. Double closed-loop resonant micro optic gyro using hybrid digital phase modulation. *Opt. Express* **23**, 15088–15097 (2015).
213 Li, J., Suh, M.-G. & Vahala, K. Microresonator Brillouin gyroscope. *Optica* **4**, 346–348 (2017).
214 Lai, Y.-H. et al. Earth rotation measured by a chip-scale ring laser gyroscope. *Nat. Photon.* **14**, 345–349 (2020).
215 Bender, C. M. & Boettcher, S. Real spectra in non-Hermitian Hamiltonians having PT symmetry. *Phys. Rev. Lett.* **80**, 5243–5246 (1998).
216 Guo, A. et al. Observation of PT-symmetry breaking in complex optical potentials. *Phys. Rev. Lett.* **103**, 093902 (2009).
217 Yu, D. & Vollmer, F. Spontaneous PT-symmetry breaking in lasing dynamics. *Commun. Phys.* **4**, 77 (2021).
218 Thompson, R. J., Rempe, G. & Kimble, H. J. Observation of normal-mode splitting for an atom in an optical cavity. *Phys. Rev. Lett.* **68**, 1132–1135 (1992).

219 Goy, P., Raimond, J. M., Gross, M. & Haroche, S. Observation of cavity-enhanced single-atom spontaneous emission. *Phys. Rev. Lett.* **50**, 1903–1906 (1983).
220 Gleyzes, S. et al. Quantum jumps of light recording the birth and death of a photon in a cavity. *Nature* **446**, 297–300 (2007).
221 McKeever, J., Boca, A., Boozer, A. D., Buck, J. R. & Kimble, H. J. Experimental realization of a one-atom laser in the regime of strong coupling. *Nature* **425**, 268–271 (2003).
222 Zheng, S.-B. & Guo, G.-C. Efficient scheme for two-atom entanglement and quantum information processing in cavity QED. *Phys. Rev. Lett.* **85**, 2392–2395 (2000).
223 Imamoglu, A. et al. Quantum information processing using quantum dot spins and cavity QED. *Phys. Rev. Lett.* **83**, 4204–4207 (1999).
224 Alton, D. J. et al. Strong interactions of single atoms and photons near a dielectric boundary. *Nat. Phys.* **7**, 159–165 (2011).
225 Mabuchi, H. & Kimble, H. J. Atom galleries for whispering atoms: binding atoms in stable orbits around an optical resonator. *Opt. Lett.* **19**, 749–751 (1994).
226 Vernooy, D. W. & Kimble, H. J. Quantum structure and dynamics for atom galleries. *Phys. Rev. A* **55**, 1239–1261 (1997).
227 Kien, F. L., Balykin, V. I. & Hakuta, K. Atom trap and waveguide using a two-color evanescent light field around a subwavelength-diameter optical fiber. *Phys. Rev. A* **70**, 063403 (2004).
228 Rosenblit, M., Japha, Y., Horak, P. & Folman, R. Simultaneous optical trapping and detection of atoms by microdisk resonators. *Phys. Rev. A* **73**, 063805 (2006).
229 Sumetsky, M. Delay of light in an optical bottle resonator with nanoscale radius variation: dispersionless, broadband, and low loss. *Phys. Rev. Lett.* **111**, 163901 (2013).
230 Sumetsky, M. & Dulashko, Y. SNAP: fabrication of long coupled microresonator chains with sub-angstrom precision. *Opt. Express* **20**, 27896–27901 (2012).
231 Wang, Y., Zeng, S., Humbert, G. & Ho, H.-P. Microfluidic whispering gallery mode optical sensors for biological applications. *Laser Photonics Rev.* **14**, 2000135 (2020).
232 Flueckiger, J., Grist, S. M., Bisra, G., Chrostowski, L. & Cheung, K. C. Cascaded silicon-on-insulator microring resonators for the detection of biomolecules in PDMS microfluidic channels. *Proc. SPIE* **7929**, 79290I (2011).
233 Persichetti, G., Grimaldi, I. A., Testa, G. & Bernini, R. Self-assembling and packaging of microbottle resonators for all-polymer lab-on-chip platform. *Sens. Actuator A Phys.* **280**, 271–276 (2018).
234 Rosenblum, S., Lovsky, Y., Arazi, L., Vollmer, F. & Dayan, B. Cavity ring-up spectroscopy for ultrafast sensing with optical microresonators. *Nat. Commun.* **6**, 6788 (2015).
235 Ye, M.-Y. & Lin, X.-M. Theory of cavity ring-up spectroscopy. *Opt. Express* **25**, 32395–32400 (2017).
236 Chen, L. Y. et al. Mass fabrication and delivery of 3D multilayer μTags into living cells. *Sci. Rep.* **3**, 2295 (2013).
237 Fernández-Rosas, E. et al. Internalization and cytotoxicity analysis of silicon-based microparticles in macrophages and embryos. *Biomed Microdevices* **12**, 371–379 (2010).
238 Cardenosa-Rubio, M. C., Robison, H. M. & Bailey, R. C. Recent advances in environmental and clinical analysis using microring resonator–based sensors. *Curr. Opin. Environ. Sci. Health* **10**, 38–46 (2019).
239 Estrada, I. A. et al. Multiplex detection of pathogen biomarkers in human blood, serum, and saliva using silicon photonic microring resonators. *Proc. SPIE* **9490**, 94900E (2015).
240 Zhu, H., Dale, P. S., Caldwell, C. W. & Fan, X. Rapid and label-free detection of breast cancer biomarker CA15-3 in clinical human serum samples with optofluidic ring resonator sensors. *Anal. Chem.* **81**, 9858–9865 (2009).
241 Wang, F., Anderson, M., Bernards, M. T. & Hunt, H. K. PEG functionalization of whispering gallery mode optical microresonator biosensors to minimize non-specific adsorption during targeted, label-free sensing. *Sensors* **15**, 18040–18060 (2015).

242 Kirk, J. T. et al. Zwitterionic polymer-modified silicon microring resonators for label-free biosensing in undiluted human plasma. *Biosens. Bioelectron.* **42**, 100–105 (2013).
243 Limpoco, F. T. & Bailey, R. C. Real-time monitoring of surface-initiated atom transfer radical polymerization using silicon photonic microring resonators: implications for combinatorial screening of polymer brush growth conditions. *J. Am. Chem. Soc.* **133**, 14864–14867 (2011).
244 Puchkova, A. et al. DNA origami nanoantennas with over 5000-fold fluorescence enhancement and single-molecule detection at 25 µM. *Nano Lett.* **15**, 8354–8359 (2015).
245 Hayat, A., Muellera, J. P. B. & Capasso, F. Lateral chirality-sorting optical forces. *Proc. Natl. Acad. Sci. U.S.A* **112**, 13190–13194 (2015).
246 Wheaton, S., Gelfand, R. M. & Gordon, R. Probing the Raman-active acoustic vibrations of nanoparticles with extraordinary spectral resolution. *Nat. Photon.* **9**, 68–72 (2015).
247 Frigenti, G. et al. Microbubble resonators for all-optical photoacoustics of flowing contrast agents. *Sensors* **20**, 1696 (2020).
248 Nezhad, M. P. et al. Room-temperature subwavelength metallo-dielectric lasers. *Nat. Photon.* **4**, 395–399 (2010).
249 Galanzha, E. I. et al. Spaser as a biological probe. *Nat. Commun.* **8**, 15528 (2017).
250 Schliesser, A. & Kippenberg, T. J. in *Advances in Atomic, Molecular, and Optical Physics* Vol. 58 (ed P. Berman, Arimondo, E. & Lin, C.) Ch. 5, 207–323 (Academic, 2010).
251 Xavier, J., Yu, D., Jones, C., Zossimova, E. & Vollmer, F. Quantum nanophotonic and nanoplasmonic sensing: towards quantum optical bioscience laboratories on chip. *Nanophotonics* **10**, 1387–1435 (2021).
252 Lam, C. C., Leung, P. T. & Young, K. Explicit asymptotic formulas for the positions, widths, and strengths of resonances in Mie scattering. *J. Opt. Soc. Am. B* **9**, 1585–1592 (1992).
253 Cai, M., Painter, O. & Vahala, K. J. Observation of critical coupling in a fiber-taper to silica-microsphere whispering-gallery mode system. *Phys. Rev. Lett.* **85**, 74–77 (2000).

Highlighted References

Vernooy, D. W., Ilchenko, V. S., Mabuchi, H., Streed, E. W. & Kimble, H. J. High-Q measurements of fused-silica microspheres in the near infrared. *Opt. Lett.* 23, 247–249 (1998). This paper presents a systematic analysis on the quality factor of a WGM microcavity.

Vollmer, F. et al. Protein detection by optical shift of a resonant microcavity. *Appl. Phys. Lett.* 80, 4057–4059 (2002). First demonstration of molecular biosensing (biotin-streptavidin) on a WGM sensor.

Vollmer, F., Arnold, S. & Keng, D. Single virus detection from the reactive shift of a whispering-gallery mode. *Proc. Natl. Acad. Sci. USA* 105, 20701–20704 (2008). First demonstration of single virus particle detection on a WGM sensor.

Zhu, J. et al. On-chip single nanoparticle detection and sizing by mode splitting in an ultrahigh-*Q* microresonator. *Nat. Photon.* 4, 46–49 (2010). This paper demonstrates the first experiment of mode-splitting-based single-particle sensing.

Baaske, M. D. & Vollmer, F. Optical observation of single atomic ions interacting with plasmonic nanorods in aqueous solution. *Nat. Photon.* 10, 733–739 (2016). This paper describes the first

experiment of single-atomic-ion detection based on the optoplasmonic sensing scheme, giving the highest sensitivity achieved to date.

Yu, W., Jiang, W. C., Lin, Q. & Lu, T. Cavity optomechanical spring sensing of single molecules. *Nat. Commun.* 7, 12311 (2016). This paper describes the first experiment of single-molecule detection based on the dynamics of an optomechanical system.

Aoki, T. et al. Observation of strong coupling between one atom and a monolithic microresonator. *Nature* 443, 671–674 (2006). This paper shows the first experiment of single neutral atoms strongly interacting with a WGM microcavity.

Baaske, M. D., Foreman, M. R. & Vollmer, F. Single-molecule nucleic acid interactions monitored on a label-free microcavity biosensor platform. *Nat. Nanotechnol.* 9, 933–939 (2014). This paper reports the first detection of biomolecular recognition between DNA oligonucleotides at the single-molecule level with a WGM.

Humar, M. & Yun, S. H. Intracellular microlasers. *Nat. Photon.* 9, 572–576 (2015). This study demonstrates several types of WGM lasers inside cells and their application for sensing and barcoding.

Chen, W., Özdemir, Ş. K., Zhao, G., Wiersig, J. & Yang, L. Exceptional points enhance sensing in an optical microcavity. *Nature* 548, 192–196 (2017). This paper demonstrates the first experiment of exceptional-point-enhanced single-particle sensing.

Kim, E., Baaske, M. D., Schuldes, I., Wilsch, P. S. & Vollmer, F. Label-free optical detection of single enzyme-reactant reactions and associated conformational changes. *Sci. Adv.* 3, e1603044 (2017). This paper demonstrates that WGMs are sensitive to conformational change of protein such as polymerase enzyme.

Martino, N. et al. Wavelength-encoded laser particles for massively multiplexed cell tagging. *Nat. Photon.* 13, 720–727 (2019). This study demonstrates tagging and tracking of thousands of cells by using single mode semiconductor disc lasers inside cells.

Schubert, M. et al. Monitoring contractility in cardiac tissue with cellular resolution using biointegrated microlasers. *Nat. Photon.* 14, 452–458 (2020). This study is one of the first ones to demonstrate WGM sensing in vivo, specifically measuring beating of heart muscles via changes in WGM spectra.

Iqbal, M. et al. Label-free biosensor arrays based on silicon ring resonators and high-speed optical scanning instrumentation. *IEEE J. Sel. Top. Quant.* 16, 654–661 (2010). This paper describes the first commercial microring biosensing instrument.

Robison, H. M. & Bailey, R. C. A guide to quantitative biomarker assay development using whispering gallery mode biosensors. *Curr. Prot. Chem. Biol.* 9, 158–173 (2017). This method paper details the development and optimization of immunoassays for WGM biosensors.

Wade, J. H. & Bailey, R. C. Applications of optical microcavity resonators in analytical chemistry. *Annu. Rev. Anal. Chem.* 9, 1–25 (2016). This review discusses varying optical resonator sensing platforms and highlights recent developments in sensing of biologics and other analytes using optical sensors.

Wang, Y., Zeng, S., Humbert, G. & Ho, H.-P. Microfluidic whispering gallery mode optical sensors for biological applications. *Laser Photonics Rev.* 14, 2000135 (2020). This recent review covers integration of varying WGM geometries with microfluidic systems.

Acknowledgements

F.V. would like to acknowledge funding from EPSRC (EP/R031428/1) and from The Royal Society (WRMA). M.H. would like to acknowledge funding from the European Research Council (ERC) under the European Union's Horizon 2020 research and innovation programme (grant agreement No. 851143) and from the Slovenian Research Agency (ARRS) (N1-0104, J1-1697 and P1-0099). R.C.B would like to acknowledge funding from US National Institutes of Health and National Institute of Allergy and Infectious Diseases (NIAID) AI141591. S.N.C. would like to acknowledge funding from the Okinawa Institute of Science and Technology Graduate University (OIST).

Author contributions

Introduction (D.Y., S.N.C and F.V.); Experimentation (D.Y., M.H., K.M., R.C.B., S.N.C and F.V.); Results (D.Y., M.H., K.M., R.C.B., S.N.C and F.V.); Applications (D.Y., M.H., S.N.C and F.V.); Reproducibility and data deposition (M.H., K.M., and R.C.B.); Limitations and Optimizations (D.Y., M.H., K.M., R.C.B., S.N.C and F.V.); Outlook (D.Y., M.H., S.N.C and F.V.); Overview of Primer (F.V.). All authors discussed and edited the full manuscript.

Competing interests

The authors declare no competing interests.

Peer review information

Nature Reviews Methods Primers thanks [Referee#1 name], [Referee#2 name] and the other, anonymous, reviewer(s) for their contribution to the peer review of this work.

Glossary

Total internal reflection: An optical phenomenon in which the light is completely reflected when it is incident from a more dense medium into a less dense medium.

Evanescent field: An oscillating electric field whose amplitude rapidly decays in a certain spatial direction, resulting in no power transport.

Effective mode volume: A volume that measures the spatial confinement of the electromagnetic energy of a cavity mode.

Quality factor: 2π times the ratio of the optical energy stored in an interferometer to the energy dissipated per electromagnetic oscillation of the light wave.

Purcell factor: The enhancement factor of the spontaneous emission rate of a photon emitter located inside an optical cavity.

Finesse: The number of round trips for a light ray travelling inside an optical resonator before escaping from the resonator in a dissipative manner.

Plasmonic hotspot: The region near sharp corners and tips of metal nanoparticles. Within this region, the electric field is strongly boosted due to the localized surface plasmon resonance.

Optical gain: A measure of a medium transferring part of its energy to a light field through the stimulated emission.

Barcoding: An operation of labelling individual cells with a unique (optical or non-optical) barcode, enabling tracking of cells and investigation of heterogeneous cell populations.

Quasi-droplet regime: A regime related to the shell thickness of a microbubble, where the shell starts to lose the ability to confine WGMs.

Optofluidic resonators: Optical microcavities whose materials are partially or completely fluid.

Degenerate: A group of cavity modes having the same resonance frequency.

Polarizability: A measure of the ability of a dielectric particle (such as an atom or molecule) to acquire an electric dipole moment when subjected to an electric field..

Rayleigh scattering: Elastic scattering of electromagnetic radiation by tiny particles whose size is much smaller than the radiation wavelength.

Dielectric nanoparticles: Small objects that are made of electrical insulators and have a size of $1\sim10^2$ nm.

Beat frequency: The difference in frequency of two electromagnetic waves with close oscillation frequencies and the stable phase difference.

Localized surface plasmon resonance: An optical phenomenon occurring when light interacts with metal nanoparticles whose sizes are much smaller than the light wavelength. The incident light drives the collective oscillation of surface electrons in the conduction band of metal nanoparticles.

Ohmic losses: The energy losses due to heat generation when electrons pass through a conductor.

Exceptional points: The singularities in the spectrum of a nonconservative system. Around a singularity point, the system responds strongly to a small perturbation.

Lasing threshold: The minimum pump intensity at which stimulated emission dominates over spontaneous emission. Above the threshold, the emission intensity as a function of the pump intensity increases much more rapidly.

Waveguides: Geometrical structures capable of confining and directing the propagation of electromagnetic or sound waves.

Noise spectral density: The energy distribution of a noise time series in the frequency domain.

Quantum shot noise: A type of noise that arises from the discrete nature of particles such as electrons and photons. The arrivals of particles at a counter satisfy a Poisson process.

Susceptibility: A dimensionless proportionality constant of a material in response to an applied electric/magnetic field.

Heisenberg uncertainty: The fundamental limit imposed by quantum mechanics. The standard deviations $\Delta A = \sqrt{\langle \hat{A}^2 \rangle - \langle \hat{A} \rangle^2}$ and $\Delta B = \sqrt{\langle \hat{B}^2 \rangle - \langle \hat{B} \rangle^2}$ of two operators $\hat{A}$ and $\hat{B}$ satisfy $\Delta A \Delta B \geq |\langle \hat{C} \rangle|/2$ with $\hat{C} = -i(\hat{A}\hat{B} - \hat{B}\hat{A})$.

Balanced homodyne detection: An approach of measuring the phase dependent quadrature of a signal, where the signal and local oscillator have the same oscillation frequency and two photodetectors are applied to eliminate the excess noise of the local oscillator.

Receptor-ligand binding: An attractive interaction, for example ionic bonds, hydrogen bonds and Van der Waals forces, between signalling (ligand) and receiving (receptor) molecules.

Forster resonance: A distance-dependent nonradiative energy transfer between a fluorescent molecule in its electronic excited state and a ground-state fluorescent molecule.

Sagnac interference: The change of the interference between a pair of laser beams, which counter propagate along a closed loop, under the rotation of the optical path loop.

Sagnac loop: A closed optical path loop for the interference between two counter-propagating laser beams.

Angle random walk: The angular error that originates from the white noise in angular rate and measures the short-term stability of a gyroscope.

Bias drift: The zero-rate output (i.e., a gyroscope in the absence of rotation) that measures the long-term stability of the gyroscope.

Hermicity: The quality that a complex square matrix or an operator in quantum mechanics is equal to its own conjugate transpose.

Parity-time-symmetric optical system: Optical systems composed of photonic components (such as waveguides and microcavities) that ensure the balance of optical gain and loss in space-reflection-related regions.

Nonreciprocity: An optical property that the light beam cannot follow its original forward path in a backward fashion.

Vacuum Rabi splitting: Mode splitting resulting from the strong coupling between a quantum emitter and a quantized cavity mode in the vacuum state, where the total energy is only one quantum.

Microspotting: A direct-contact-based technique that deposits biomolecules on a solid surface.

Thermorefractive noise floor: The fluctuations of the cavity resonance frequency resulting from the fluctuations of temperature acting on the refractive index of the optical cavity material.